

Modeling high-entropy transition-metal alloys with alchemical compression

Nataliya Lopanitsyna,¹ Guillaume Fraux,¹ Maximilian A. Springer,² Sandip De,² and Michele Ceriotti¹

¹*Laboratory of Computational Science and Modeling, Institute of Materials,*

École Polytechnique Fédérale de Lausanne, 1015 Lausanne, Switzerland

²*BASF SE, Carl-Bosch-Straße 38, 67056 Ludwigshafen, Germany*

Alloys composed of several elements in roughly equimolar composition, often referred to as high-entropy alloys, have long been of interest for their thermodynamics and peculiar mechanical properties, and more recently for their potential application in catalysis. They are a considerable challenge to traditional atomistic modeling, and also to data-driven potentials that for the most part have memory footprint, computational effort and data requirements which scale poorly with the number of elements included. We apply a recently proposed scheme to compress chemical information in a lower-dimensional space, which reduces dramatically the cost of the model with negligible loss of accuracy, to build a potential that can describe 25 d -block transition metals. The model shows semi-quantitative accuracy for prototypical alloys, and is remarkably stable when extrapolating to structures outside its training set. We use this framework to study element segregation in a computational experiment that simulates an equimolar alloy of all 25 elements, mimicking the seminal experiments by Cantor et al., and use our observations on the short-range order relations between the elements to define a data-driven set of Hume-Rothery rules that can serve as guidance for alloy design. We conclude with a study of three prototypical alloys, CoCrFeMnNi, CoCrFeMoNi and IrPdPtRhRu, determining their stability and the short-range order behavior of their constituents.

I. INTRODUCTION

Almost 20 years have passed since independent work from the groups of Yeh¹ and Cantor² showed that mixing up to 20 metallic elements in roughly equal parts leads to a smaller-than-expected number of distinct phases, with some corresponding to disordered solid solutions of 4-6 elements. These so-called high-entropy alloys (HEAs) have since become the subject of intense study.³ On a fundamental level, the observation of the existence of an extended single-phase stability region for alloys with multiple principal components was surprising, and from a technological standpoint it opened up the possibility of designing new materials that defy the limitations of conventional metallurgy and alloy engineering.^{4,5}

Besides their metallurgical and mechanical applications, HEAs have been found to be promising catalysts^{6,7}, especially in electrocatalysis⁸⁻¹⁰. They can efficiently reduce overpotentials and boost activities for, e.g., water splitting¹¹⁻²¹, the oxygen reduction reaction^{15,18,22-24}, or the methanol oxidation reaction^{22,25-28} while exhibiting very good stability under reaction conditions. These unusual properties are linked to their multi-elemental character, which gives rise to four core effects^{29,30}: the entropy, 'sluggish diffusion', lattice distortion and 'cocktail effect'. While the former two enhance the stability, the latter two can explain the high activity in catalysis. First, lattice distortions occur due to atoms being surrounded by atoms of many different atomic radii leading to stress and strain. This alters the electronic structure of the alloy. For example, the water splitting activity of a family of AlNiCoIrX (X = Mo, Cr, Cu, Nb, V) is superior to IrO₂ because the lattice distortion leads to shorter Ir-O bonds¹⁴. Second, the 'cocktail effect' describes unexpected, synergistic effects of

the chosen composition. For instance, the non-noble metal HEA CoCrFeMoNi shows activity for the oxygen reduction reaction similar to that of Pt.

From the computational perspective, modeling HEAs poses a number of distinct challenges. The presence of multiple components requires relatively large simulation cells to unveil microstructures or order-disorder behaviour, while the sluggish diffusion requires long time scales and accelerated sampling techniques to overcome free-energy barriers to atom diffusion. Chemical complexity makes empirical forcefields inaccurate, and sampling issues make explicit electronic-structure calculations prohibitively demanding. As a consequence, the study of HEAs usually relies on on-site cluster expansions^{31,32}, together with analytical models that allow to capture the qualitative thermodynamic behavior³³, even though entropic effects beyond configurational ones are known to play an important role.³⁴ More recently, forcefields based on machine learning (ML) have emerged as an alternative approach, allowing to match the accuracy of first-principles calculations, while describing off-lattice distortions and thermal fluctuations³⁵⁻³⁸. However, the majority of ML frameworks for materials modeling exhibit a poor scaling of memory, computation and data requirements with the number of chemical species, and so simulations this far have been restricted to a specific combination of 4-5 elements. In this paper we introduce a general-purpose ML model for the study of bulk HEAs, that uses a recently-proposed strategy to reduce the dimensionality of chemical space, allowing us to generate an accurate and transferable ML potential that can describe arbitrary mixtures of 25 transition metals. The functional form of the model lends itself to an intuitive interpretation of the relations between different transition metals, and careful validation shows

that it is capable of accuracy comparable to that of electronic-structure methods in several reference calculations despite the breadth of chemical space it covers. We use this potential to reproduce computationally the seminal Cantor experiments on the decomposition of multi-element mixtures, and find a qualitative behavior in the affinity between different species that is consistent with well-known HEAs, allowing us to introduce a data-driven version of the Hume-Rothery rules to guide alloy design. We conclude by studying three alloy compositions - the prototypical Cantor alloy CoCrFeMnNi, its Mn→Mo counterpart that has enhanced catalytic performance, and PdPtIrRuRh - another promising composition for catalysis. In all cases we observe a tendency to phase-separate at low temperature, and that the short-range order observed in high-temperature conditions is indicative of the thermodynamic drive to de-mix.

II. ALCHEMICAL COMPRESSION OF ML REPRESENTATIONS

We follow the approach introduced in Ref. 39 to reduce the computation, memory and data requirements of a ML model for a chemically-diverse problem. Here we only give a brief overview, to highlight the key ideas and introduce the notation. The framework relies on the atom-centered density correlation framework⁴⁰, which encompasses most of the widespread descriptors for atomic-scale ML, and that is essentially equivalent to the moment tensor potentials⁴¹ and the atomic cluster expansion⁴². The reader is invited to read Ref. 43 (especially Sections 3 and 7.3) for a more pedagogic discussion. The essential ingredient in this framework is the expansion of the neighbor density within an environment A_i , that describe the atoms in structure A within a spherical region centered on the i -th atom (Fig. 1a, on a basis of radial functions R_{nl} and spherical harmonics Y_l^m):

$$\begin{aligned} \langle anlm|\rho_i \rangle &= \int d\mathbf{x} R_{nl}(x) Y_l^m(\hat{\mathbf{x}}) \langle a\mathbf{x}|\rho_i \rangle, \\ \langle a\mathbf{x}|\rho_i \rangle &\equiv \sum_{j \in A_i} \delta_{aa_j} g(\mathbf{x} - \mathbf{r}_{ji}). \end{aligned} \quad (1)$$

In this expression, j runs over the neighbors of atom i , $g(\mathbf{x})$ is a Gaussian function (or its Dirac- δ limit), $\mathbf{r}_{ji} \equiv \mathbf{r}_j - \mathbf{r}_i$ is the interatomic distance vector between the j -th and i -th atom, R_{nl} enumerates the radial functions and Y_l^m the spherical harmonics. The ket $|\rho_i \rangle$ indicates the i -centered neighbor density and the a index identifies the chemical nature of the atoms.

The bra-ket notation serves to emphasize the fact that the discrete coefficients are simply a projection on a basis of the very same quantity as the real-space neighbor density. We also express the density coefficients with the alternative notation $\langle an|\rho_i^{\otimes 1}; \lambda\mu \rangle \equiv \langle an\lambda\mu|\rho_i \rangle$, in which $\rho_i^{\otimes \nu}$ indicates we are describing the ν -neighbors density correlations, and the angular indices (λ, μ) are moved to the ket to highlight

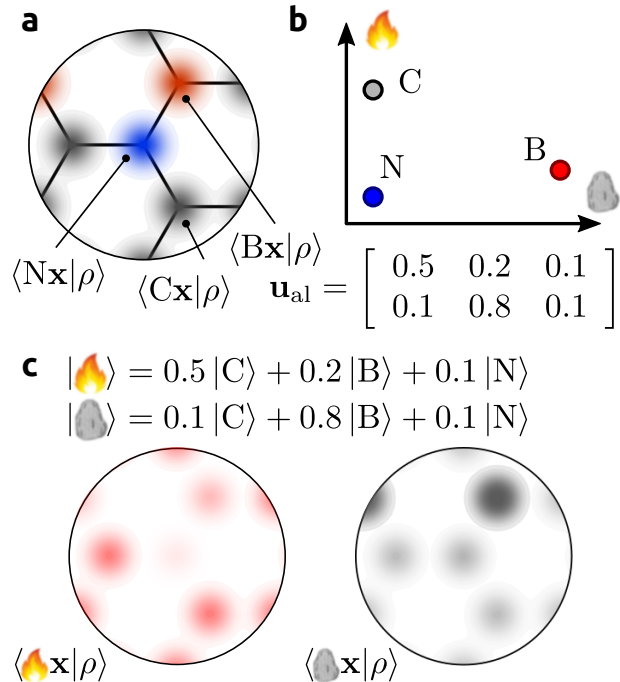


Figure 1. Different interpretations of the alchemical compression scheme. (a) In a conventional density-correlation ML scheme, each type of atoms is associated with a separate density. (b) The entries in the alchemical compression matrix \mathbf{u}_{alch} can be interpreted as describing the “character” of each physical element in terms of n_{alch} pseudoelements - a concept that is not dissimilar from the notion of “classical elements”. (c) The structure can be also seen as described in terms of a density of pseudo-elements, for which each site contains a contribution from each of the compressed channels.

that they determine the symmetry of the coefficients with respect to rotations, that is crucial when building equivariant models and when combining density coefficients to evaluate higher-order correlations.

In this work we will use the pair invariants ($\nu = 1$, $\lambda = 0$, i.e. $\langle an|\rho_i^{\otimes 1} \rangle \equiv \langle an|\rho_i^{\otimes 1}; 00 \rangle$), as well as the two-neighbors invariant terms ($\nu = 2$, $\lambda = 0$). The two-neighbors invariants — equivalent to SOAP features⁴⁴ and closely-related to three-body Behler-Parrinello symmetry functions⁴⁵ — can be computed as:

$$\begin{aligned} \langle a_1 n_1; a_2 n_2; l|\rho_i^{\otimes 2} \rangle &\propto \sum_m \langle a_1 n_1|\rho_i^{\otimes 1}; lm \rangle \\ &\quad \times \langle a_2 n_2|\rho_i^{\otimes 1}; lm \rangle. \end{aligned} \quad (2)$$

For readers familiar with the notation used in the SOAP literature⁴⁴, the expansion coefficients of the density are often written as c_{nlm}^a and the power spectrum, corresponding to the two-point correlations (2), as $p_{n_1 n_2 l}^{a_1 a_2}$. In both forms, it is clear that the number of components one has to consider grows quadratically with the number of species, each element being considered independently in the neighbor density. The generalization to higher- ν correlations leads to an

even steeper increase, but for the dataset we consider here, the computational cost is prohibitive even for two-neighbors correlations.

The key insight in Ref. 39 is that it is unnecessary — and possibly detrimental — to consider elements as independent. Similarities in the behavior of elements have inspired the construction in the periodic table,⁴⁶ and are routinely used to inform materials design and optimization. Instead, elements should be mapped to a continuous n_{alch} -dimensional space, where each chemical species is mapped to n_{alch} *pseudo-species* with a set of coupling coefficients \mathbf{u}_{alch} . Then, the density coefficients can be contracted as

$$\langle bn | \overline{\tilde{\rho}_i^{\otimes 1}}; \lambda\mu \rangle \equiv \sum_a u_{ba} \langle an | \overline{\rho_i^{\otimes 1}}; \lambda\mu \rangle, \quad (3)$$

where we use $\tilde{\rho}$ to indicate the alchemically-compressed neighbor density (Fig. 1). We note that similar ideas were applied — without optimizing the contraction coefficients — in the context of atom-centered symmetry functions^{47,48}, and that a systematic, rather than data-driven, compression has also been recently applied to a 8-element alloy system in the context of atomic cluster expansion potentials⁴⁹. Moreover, there is a large design space of variations on a theme: separate coupling coefficients could be used depending on angular (λ) and/or radial (n) channel, and it would be possible to jointly contract over chemical and radial components — which was shown to be effective in reducing the number of features with minimal information loss⁵⁰. Here we do not explore this design space, because, as we shall see, the pure alchemical contraction appears to be both effective and easy to interpret. Using these compressed density coefficients (3) one can evaluate correlation functions with a cost that still scales exponentially with ν , but with a more benign base, or perform further iterative contraction steps as in Ref. 51.

To conclude this overview, we note that the alchemical coefficients \mathbf{u}_{alch} enter the expression for the $\nu = 2$ features in a quadratic fashion, and so they cannot be directly determined using linear algebra, even if one uses a linear model based on the contracted features. In Ref. 39 this issue was tackled with an iterative strategy, alternating a solution of the linear problem with fixed \mathbf{u}_{alch} and a gradient descent on the coupling coefficients. In the present work, instead, we implement the model using the PyTorch framework⁵², allowing us to use automatic differentiation and gradient descent to optimize simultaneously \mathbf{u}_{alch} and the model weights.

III. COMPUTATIONAL DETAILS

We provide a concise summary of the details of the calculations we perform in this work, covering the reference electronic-structure calculations, the construction of the training set, the architecture of the ML model, as well as the details of the sampling protocol

that we use for simulations in Sections VI and VII. In the Supplemental Material¹⁰³ we provide representative examples of the typical simulation setup, and additional convergence tests.

A. Electronic-structure details

All the reference energies and forces are computed using density-functional theory (DFT), as implemented in the VASP code⁵³, with the PBEsol exchange-correlation functional⁵⁴. The core electrons are treated implicitly using projector augmented wave (PAW) pseudopotentials⁵⁵. We choose conservative values for the convergence parameters of the electronic structure calculation (see the Supplemental Material¹⁰³ for details): the wave function is expanded in plane waves with a cutoff energy of 550 eV, and the Brillouin zone sampling uses a Γ centered Monkhorst-Pack scheme⁵⁶ with an interval between k-points along reciprocal lattice vector $0.04 \pi \text{ \AA}^{-1}$. Even though transition metals often exhibit magnetism, either in the pure phases or in alloys, we perform all our calculations without spin polarization. Even disregarding the fact that ML models that can deal with magnetism are still at a very early stage⁵⁷, one should consider that we aim to cover a broad chemical range, that includes materials which require different types of approaches to describe accurately their magnetic behavior - band magnetism within the local spin density approximation,⁵⁸ non-collinear magnetism,⁵⁹ Hubbard-U calculations⁶⁰, etc. This makes non-polarized calculations a reasonable approximation within the scope of the present work (see also the Supplemental Material¹⁰³), even though this limits the accuracy of our reference and our model for magnetic systems - which for example would not be able to predict the stabilization of *bcc* iron over the close-packed polymorphs.

B. Training set construction

We generated an original dataset including 25 d -block elements, i.e. all transition metals excluding those that are not listed in Ref. 61 as relevant for HEAs (Tc, Cd, Re, Os, Hg). We generate a total of 25 thousand structures, following a protocol that ensures quasi-random sampling of this high dimensional phase space. We created four subsets of structures based on *bcc* and *fcc* lattices containing 36 or 48 atoms, respectively. All lattice parameters are defined by the average atomic volume of the elements in a structure and scaled up or down by up to 10% at random to simulate compression and expansion. The structures in the first three classes include from 3 to 8 randomly selected elements, and in the fourth — from 3 to 25. In the first class, we included only perfect crystal structures, with random compositions. For the three remaining classes, we shuffled atomic positions around their ideal lattice sites (using a Gaussian distribution

of atomic displacement with a standard deviation of 0.2 Å in the second and fourth classes, and 0.5 Å in the third), to incorporate the information about interactions in crystals at finite temperatures.

For every class of structures, we generated 100'000 random configurations and selected around 7'000 of the most diverse from every subset using Farthest Point Sampling (FPS)⁶² in radial spectrum feature space.

C. Machine-learning model

We build ML models based on density-correlation representations, combining an atomic-energy baseline, ridge regression based on pair and 3-body correlation features, and a multi-layer perceptron⁶³ based on the 3-body features. Here we discuss briefly the functional form of the different term, and outline the training strategy we followed. The atomic-energy baseline is simply a linear model that depends exclusively on the nature of the atom at the centre of each environment, a_i

$$V^{(\text{aeb})}(A_i) = w_{a_i}^{(\text{aeb})}. \quad (4)$$

Even though we train on atomization energies (and so the large dependency of the atomic energies on the details of the pseudopotentials is not an issue) we still find that $V^{(\text{aeb})}$ captures a large fraction of the target variance, and facilitates learning. The second term we consider is a set of pair energies. We use a Gaussian width of 0.25Å, a cutoff of 6Å and radial scaling following Ref. 39; we expand the density in spherical harmonics and in 12 radial function, enumerated by the n index, and obtained by orthogonalizing Gaussian-type orbitals that cover the range of distances up to the cutoff radius (see e.g. Ref. 64 for a precise definition). We use different weights depending on the nature of the two atoms, so that in practice the contribution to the potential reads

$$V^{(2\text{B})}(A_i) = \sum_{an} w_{a_i an}^{(2\text{B})} \langle an | \overline{\rho_i^{\otimes 1}} \rangle. \quad (5)$$

The third term involves 3-body correlations (SOAP features), computed on top of alchemically-contracted density coefficients, with a linear model

$$V^{(3\text{B})}(A_i) = \sum_{bnb'n'l} w_{bnb'n'l}^{(3\text{B})} \langle bnb'n'l | \overline{\rho_i^{\otimes 2}} \rangle. \quad (6)$$

We use the same set of weights irrespective of the atom type, because in a 3-body descriptor the nature of the central atom is encoded in the density associated with the Gaussian at $r = 0$, so that the compression of the dependency of potentials on the central atom type is achieved implicitly and with the same contraction coefficients used for the neighbor density.

Finally, we include a non-linear term that takes the compressed power-spectrum as input, and feeds it into a Behler-Parrinello-style⁶⁵ multi-layer perceptron⁶³.

First, a linear filter projects the power-spectrum features into 80 input neurons, $\xi^{(0)}$, to which hyperbolic tangent activation functions are applied. A second linear layer combines the outputs of the neurons, feeding them to one hidden layer of the same size. Finally, the outputs are linearly combined to yield the atomic energy

$$\xi_q^{(0)}(A_i) = \sum_{bnb'n'l} w_{bnb'n'l}^{(NN,0)} \langle bnb'n'l | \overline{\rho_i^{\otimes 2}} \rangle, \quad (7)$$

$$V^{(\text{NN})}(A_i) = F(\xi^{(0)}(A_i))$$

We use this simple neural network — built on top of the compressed power-spectrum features — because we want a simple and well-understood term that can incorporate non-linearity without exploding the design space, and because we want to show that our alchemical compression scheme can be readily applied to several well-established ML schemes. It is possible (and likely) that alternative frameworks, e.g. increasing further the body order, may allow for a better-performing model, but as we shall see this approach is sufficient to achieve state-of-the-art accuracy together with a stable and interpretable model.

The parameters of $V^{(3\text{B})}$ and $V^{(\text{NN})}$ implicitly include the alchemical coupling matrix \mathbf{u}_{alch} ; for this reason, we optimize all models with gradient descent, relying on backpropagation as implemented in PyTorch⁵². A ridge penalty term is included on all weights, to reduce the risk of overfitting. We find that (possibly due to the presence of large linear components that contribute a quadratic term to the L^2 loss) a deterministic L-BFGS optimizer⁶⁶ performs much better than stochastic gradient descent.

D. Sampling details

Molecular dynamics (MD) is well-suited to describe structural relaxation of the atomic coordinates. However, long-range diffusion in the solid phase occurs through vacancies, and is too slow to be simulated explicitly by MD. To overcome this time scale problem, we use a combination of techniques to facilitate thorough sampling of atomic ordering. Our base protocol involves performing molecular-dynamics simulations in the constant-temperature/constant-pressure NpT ensemble.⁶⁷ We use a conservative time step of 2 fs, an isotropic barostat⁶⁸ with a time constant of 200 fs coupled to an optimal-sampling colored-noise thermostat⁶⁹, and an aggressive thermostat for the ions, alternating an optimal-sampling Langevin equation with a stochastic velocity rescaling⁷⁰ with a time constant of 10 fs. We accelerate sampling of the compositional (dis)order by performing Monte Carlo steps in which the nature of two atoms in the system is exchanged, with a Metropolis acceptance criterion⁷¹. We perform on average one exchange attempt per MD time step. Both the MD and the MC step conserve the Boltzmann distribution (except for a negligible finite time-step error), and so the combined

MD/MC protocol is consistent with canonical sampling. In order to further accelerate sampling, we also use replica exchange molecular dynamics (REMD)⁷² – a technique in which multiple trajectories at different temperatures are performed in parallel. Periodically, structures are exchanged between temperatures, using a Monte Carlo procedure that preserves the Boltzmann distribution for each thermodynamic state. The fact that each trajectory is brought through cycles of heating and annealing accelerates conformational sampling and reduces the correlation time of observables that are associated with activated events at low temperature. Unless otherwise specified, we use temperature replicas distributed according to a geometric progression between two extremal values T_{\min} and T_{\max} . For all MD/MC simulations we use the i-PI universal force engine⁷³, that includes an implementation of element exchange moves⁷⁴ and a flexible implementation of replica exchange⁷⁵.

IV. ALCHEMICAL LEARNING

As discussed above, the compression scheme in Eq. (3) is just one of the many approaches one could take to reduce the dimensionality of the density expansion coefficients. One of the appealing features of this specific implementation is that it can be interpreted relatively easily, and that it allows us to extract physical-chemical insights through an introspection of the model parameters and performance.

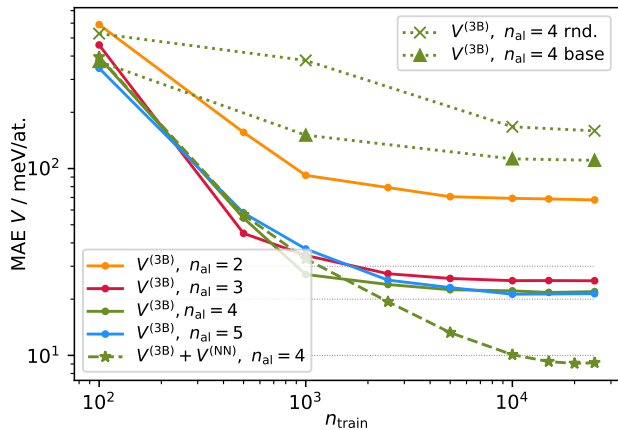


Figure 2. Learning curves for different models. Full lines correspond to models built using only $V^{(\text{aeb})}$ and $V^{(3\text{B})}$, with n_{alch} pseudo-elements (all optimized iteratively). The dotted green curves are obtained with a \mathbf{u}_{alch} filled with uniform random numbers (rnd.) and with the weights we use as an initial guess for the optimized models (base), that are built based on physical priors following the scheme discussed in Ref. 39. The dashed green line corresponds to a model that includes $V^{(\text{aeb})}$ and $V^{(3\text{B})}$, as well as the full set of pair potentials and a non-linear term built on top of the contracted power spectrum features $V^{(\text{NN})}$.

A. Learning curve analysis

We begin by considering linear models based on contracted power-spectrum features, supplemented by an atomic energy baseline term, $V^{(\text{aeb})} + V^{(3\text{B})}$. We perform separate training exercises, using only energy as targets, and restricting the alchemical contraction to 2, 3, 4, 5 pseudoelements. For each model we compute learning curves by converging the loss at a given number of training structures n_{train} , then increase the train size and continue the optimization restarting from the previous weights. Given that the optimization procedure is rather demanding, we do not perform multiple train/test split, but use consistently the same shuffle with up to 25'000 structure used for training and a hold-out set containing 500 configurations used for testing. Even though the accuracy does depend slightly on the shuffle, and on the initialization of the weights, we find that the qualitative observations we present here are robust.

Figure 2 shows a behavior similar to that observed in Ref. 39 for an analogous exercise on the elpasolites data set⁷⁶: at the smaller train set sizes a very aggressive compression is effective at obtaining a robust model, but with more training data the learning curves saturate. Increasing the number of pseudoelements n_{alch} delays saturation, but the improvement going from $n_{\text{alch}} = 3$ to $n_{\text{alch}} = 4$ is negligible, and the learning curves for $n_{\text{alch}} = 5$ sits almost exactly at the same value. This indicates that, from the point of view of 3-body interactions, 3-4 pseudo-elements are sufficient to saturate the descriptive power of a linear model. Note that the optimization of \mathbf{u}_{alch} is critical to achieve such efficient compression: a model that uses fixed, random values for the contraction weights, as well as one that uses a fixed, physically-inspired initialization of \mathbf{u}_{alch} , lead to an order of magnitude increase in the saturation error, even with $n_{\text{alch}} = 4$ (Fig. 2).

Given the saturation of $V^{(3\text{B})}$, we proceed to increase the effective body-order of the potential adding a non-linear NN layer on top of the contracted power spectrum, $V^{(\text{NN})}$, which introduces about 160'000 additional model parameters, mostly associated with the contraction of the $|\tilde{\rho}_i^{\otimes 2}\rangle$ features to the 80 input features of the NN. Furthermore, we also include a non-compressed two-body potential $V^{(2\text{B})}$, for which we also consider a slightly larger cutoff distance. This 2-body term, on its own, does not improve significantly the limiting accuracy of the model (reinforcing the notion that the alchemical contraction is converged) but we include it because it is inexpensive to compute, and has been shown in the past to lead to more stable models, whose performance degrade more gently in the extrapolative regime^{77,78}. Incorporating a non-linear term in the model allows to overcome the saturation of the learning curve (Fig. 2, dashed green line). The non-linear $n_{\text{alch}} = 4$ model reaches a validation-set mean absolute error (MAE) below 10 meV/atom. We discuss further the accuracy of this model (that

we will refer to as the HEA25-4-NN) in Section V.

B. A 3D periodic table for the transition metals

The alchemical coupling matrix associates to each of the physical elements a vector of size n_{alch} , that can be regarded as the ‘‘composition’’ of that element in terms of a set of pseudo-elements (Fig. 1b). Thus, different atomic species can be seen as points in a continuum space, and can be visualized as such to gain insights into the data-driven similarities that arise from the optimization of \mathbf{u}_{alch} to achieve the most accurate regression of the target. To make the visualization independent on unitary transformations of the weight matrix, we perform a principal component analysis.

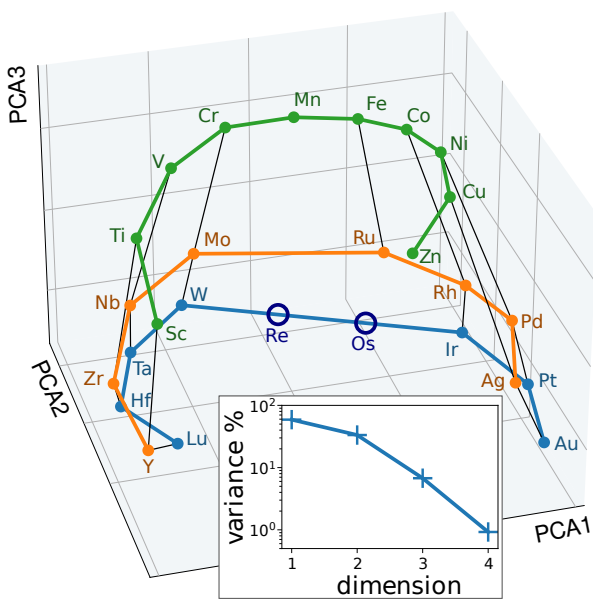


Figure 3. Top-3 principal components of the alchemical coupling matrix \mathbf{u}_{alch} for the HEA25-4-NN model. The periods are highlighted with orange, blue and green lines, and the columns are indicated by black thin lines. Interpolated positions for Re and Os are indicated with empty circles. The inset shows the decay of the explained variance for the four principal components.

The eigenvalues of the covariance matrix indicate the magnitude of the various components (their *explained variance*), and provide another indication of the importance of successive increases in the dimensionality of the alchemical space. We observe a quick decrease of the explained variance, with the fourth component typically amounting to less than 2% of the variance (Fig. 3, inset). This confirms that the first three components provide sufficient descriptive power to capture the difference in behavior between transition metals. We can then look at how the d -block elements appear when projected along the top three principal components of \mathbf{u}_{alch} (Fig. 3). We focus on the weights from the HEA25-4-NN model, but the qualitative features of the alchemical projections are similar also for other models in Fig. 2 (see the Supple-

mental Material¹⁰³). The elements are arranged in a way that is strongly reminiscent of their placement in the d block: the third principal direction corresponds to the period, while the first two dimensions are associated with a semicircular arrangement, with the elements appearing in the same order as the columns in the conventional periodic table. Interestingly, this arrangement is reminiscent of that used for the d block in some of the alternative representations of the periodic table, such as the Benfey spiral⁷⁹. It indicates that, from the point of view of the construction of an interatomic potential, zinc is closer to scandium than it is to the atoms in the middle of the transition metals block.

C. Alchemical interpolation

The elements we have not considered leave a clear gap in the arrangement of the alchemical coupling weights, and it is interesting to see how accurate a model that places rhenium and osmium between tungsten and iridium fares in predicting their properties without additional fitting.

We pick 60 structures from the hold-out set, containing distorted configurations with random composition. The MAE for these structures when using the $n_{\text{alch}} = 4$ model using only $V^{(\text{aeb})}$ and $V^{(3\text{B})}$ is 13 meV/atom. We then substitute some random atoms with Re and Os, without changing the positions, and re-compute their energies with analogous DFT settings.

We then build a model in which we simply take the parameters optimized for the 25-elements dataset, and complete them by adding atomic-energy baselines for Re and Os (obtained by training on the residual a two-parameter model that depends exclusively on the Re and Os content) and by adding pseudoelement weights that interpolate linearly between W and Ir (see Fig. 3):

$$u_{\text{bRe}} = \frac{2}{3}u_{\text{bW}} + \frac{1}{3}u_{\text{bIr}}, \quad u_{\text{bOs}} = \frac{1}{3}u_{\text{bW}} + \frac{2}{3}u_{\text{bIr}}. \quad (8)$$

The powerspectrum model weights are unchanged: we are effectively interpolating in pseudoelement space. The the resulting model yields exactly the same predictions for structures that do not contain Os and Re, and has a MAE of only 24 meV/atom for the test structures that include the two species (see also the Supplemental Material¹⁰³). The model is also sufficiently stable to run molecular dynamics simulations for Re and Os containing structures.

This example underscores the advantages of the interpretable functional form we use to implement alchemical dimensionality reduction. It also opens up the possibility of designing simulation protocols that include smooth ‘‘alchemical transformations’’, in a similar spirit as the framework pioneered by von Lilienfeld et al.⁸⁰, and with some similarities to the virtual crystal approximation that is often used to

describe approximately random alloys⁸¹. For example, one could use thermodynamic integration to compute the change in chemical potential associated with an element substitution by running simulations with a mixed potential, in which the alchemical coupling weights are gradually transformed between the values associated with two elements.

V. VALIDATION OF THE POTENTIAL

We now assess the accuracy and stability of the model we use in the rest of this work, which combines a 4-pseudoelement contraction of the power-spectrum with a multi-layer perceptron. We aim to provide benchmarks that are easy to reproduce, but that reflect the performance of the model in relevant simulation tasks, and we envisage that any comparative study would include most of these and not only cross-validation statistics. To contextualize and provide a reference scale for our results, we report in the Supplemental Material¹⁰³ similar validation results for the general-purpose, universal graph neural network M3GNet⁸². In all cases HEA25-4-NN, which admittedly has a narrower scope of applicability, outperforms M3GNet by a large margin.

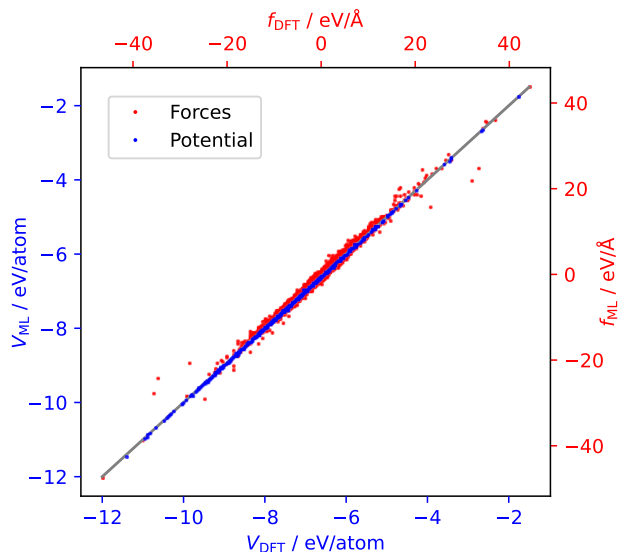


Figure 4. Parity plot between reference energy and forces and the values computed with the HEA25-4-NN model, for a hold-out set of 500 structures, randomly selected from the overall pool of structures. Energy error: 10 meV/atom mean absolute error (MAE), 14 meV/atom root mean square error (RMSE), Force error: 190 meV/Å MAE, 280 meV/Å RMSE.

A. Hold-out validation of the HEA25-4-NN model

We train the HEA25-4-NN potential by progressively increasing the train set size, until we run the final optimization on 25'000 structures, including forces

for 2'000 of them. We hold out 500 structures and use them for validation. The parity plot between targets and predictions demonstrates the accuracy of the model (Fig. 4), which is remarkable given the diversity of the dataset, that contains random combinations of up to 25 elements, and highly-distorted structures.

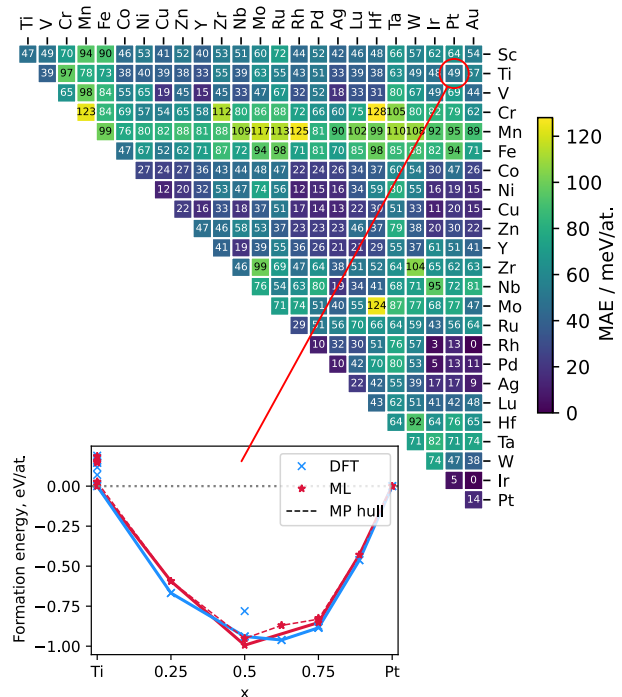


Figure 5. MAE for the formation energy of binary compounds from the Materials Project database. The inset shows a representative hull plot for the Ti-Pt system, highlighting the hulls obtained from the single-point DFT calculations and the ML predictions. The dashed line identifies the structures that are stable based on the energies available in the Materials Project database.

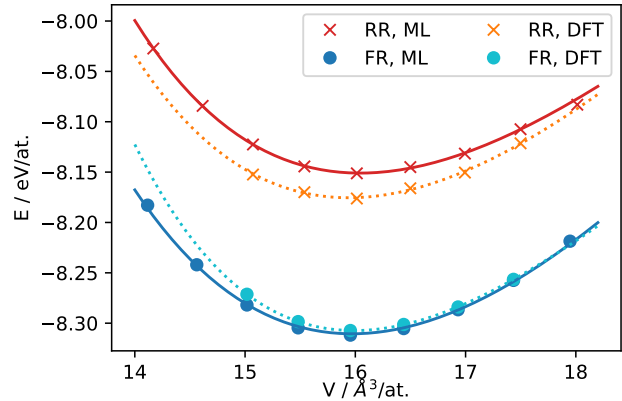
B. Binary convex hulls

Even though the HEA25-4-NN is clearly geared towards multi-component simulations, it is important that it also provides reasonable results for simpler compositions, as these may appear spontaneously when complex alloys de-mix and form precipitates. We collect 1438 binary intermetallic structures out of more than 146k crystal structures from the Materials Project database⁸³, and re-compute their energies with single-point calculations using our DFT setup, as well as with the HEA25-4-NN model. We discard 23 structures for which our DFT calculations did not converge and 10 that correspond to configurations that are too dissimilar from the bulk structures we consider here (see Supplemental Material¹⁰³). For the remaining structures, the MAE error for the cohesive energy is 62 meV/at. and for the formation energies is 63 meV/at, which is higher than the cross-validation error, but still remarkably accurate for extrapolative

predictions. It is worth noting that the MAE discrepancy between our DFT calculations and those saved in the MP records is 65 meV/at.; this is due to the significant difference in the details of the electronic structure calculations, e.g. the use of Hubbard U corrections for some structures in the MP protocol, and neglect of spin polarization in ours. This observation underscores that the details of the electronic structure calculations can have an impact comparable to the accuracy of our ML model. We then use this data to compute binary convex-hull diagrams for all element pairs. In Fig. 5 we show a representative example for the Ti-Pt system. The overall shape of the hull is usually well-reproduced, but often HEA25-4-NN predicts different stable polymorphs than DFT, and/or mis-predicts the stability of certain compositions (as it is the case for TiPt_2 in the figure). However, these qualitative errors are usually associated with situations in which a small energy shift can bring a composition above the hull boundary, and even in a fully ab initio study it would not be possible to determine conclusively its thermodynamic stability. The full list of hulls is included in the Supplemental Material¹⁰³. Fig. 5 also shows an overview of the accuracy of the prediction of formation energies for all phases (stable and unstable) as a function of composition. Errors are not uniform: some elements such as Mn, that have the tendency of forming complex crystal structures, yield larger errors, while others such as Cu or Ni usually yield errors comparable to the validation set. It would be trivial to improve the accuracy of the model for binary structures and pure element polymorphs by including this small number of additional structures in the training set. We chose not to do that to avoid introducing biases in the accuracy depending on the different abundance of structures in the MP database. In the future, we plan to extend systematically our training set to incorporate disordered and liquid structures.

C. Energy and equation of state

We prepare a $5 \times 5 \times 5$ *fcc* supercell, containing 5 atoms of each of the 25 elements, arranged randomly on the lattice. We relax the geometry of the structure, and the volume of the supercell, using the HEA25-4-NN potential. We refer to this structure as the random relaxed (RR) structure. Starting from the same configuration, we also perform a slow annealing trajectory, combining molecular dynamics and atom exchange moves, to obtain a structure in which the arrangement of elements is not random, but more energetically favorable. We refer to this structure as the fully-relaxed (FR) structure. In both cases, the atoms relax away from *fcc* lattice positions, and the resulting structure within the supercell is rather disordered. We then introduce an isotropic compression or expansion of the two structures, relaxing the coordinates of the atoms within the cell, and fit a Birch-Murnaghan equation of state to the resulting



	RR, ML	RR, DFT	FR, ML	FR, DFT
E_0 (eV/at.)	-8.151	-8.175	-8.310	-8.307
V_0 ($\text{\AA}^3/\text{at.}$)	16.04	15.94	15.97	16.00
B_0 (GPa)	132	141	146	162
B'_0	6.7	6.1	4.8	8.0

Figure 6. Equation of state for the random relaxed (RR) and fully relaxed (FR) structures (see text for the full definition), computed with the HEA25-4-NN potential and with the reference DFT. Birch-Murnaghan parameters for cohesive energy (E_0), equilibrium volume (V_0), bulk modulus (B_0), bulk modulus derivative (B'_0) are given in the table.

energy-volume curves. We repeat the fixed-cell relaxation with the reference DFT, and compare the resulting equations of state (Fig. 6). The error on the cohesive energy E_0 is comparable to the test error (24meV for $E_0^{(\text{RR})}$, 3meV for $E_0^{(\text{FR})}$), and much smaller than the energy gain associated with the annealing of the lattice occupations ($E_0^{(\text{RR})} - E_0^{(\text{FR})}$ is about 150 meV/atom), indicating that HEA25-4-NN is reliable for assessing the energetics of ordering in a random alloy. The equilibrium volume and bulk modulus for the two structures are also in good agreement, with errors below 1% and 10 %, respectively – comparable with the typical discrepancy between different DFT approximations or between DFT and experiments.

D. Molecular dynamics

As a further demonstration of the accuracy and the stability of this potential, we perform two constant-pressure MD/MC trajectories, one at $T = 300\text{K}$ and one at $T = 5000\text{K}$, each starting from a random arrangement of 5 atoms for each of the 25 elements (a total of 125 atoms) arranged on an *fcc* lattice. The trajectories are 10ps long, with on average one attempt at exchanging a pair of atoms every 2fs. We save a configuration every 100fs, and perform DFT calculations to compare energy and forces with those obtained from the ML potential. Fig. 7 shows that the low-temperature trajectory, where major rearrangements of the atoms occur but the structure remains approx-

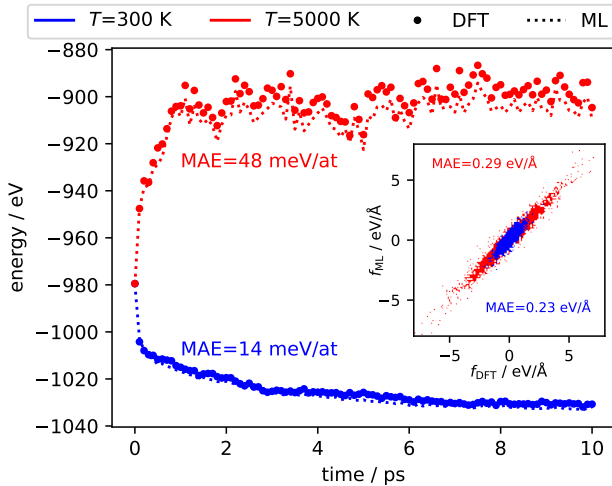


Figure 7. Comparison between the potential energy evaluated along two 10ps MD/MC trajectories, and that recomputed by DFT for 100 snapshots. The inset shows the parity plot for the force components computed for those structures. Energies have a MAE of 14 (48) meV/atom and forces a component MAE of 0.23 (0.29) eV/Å for the 300 (5000) K trajectory.

imately *fcc*, has an accuracy comparable to that measured on the validation set. The high-temperature run exhibits a higher error. However, the main component of the error is a rigid shift of the energies, and the trajectory remains stable – which is remarkable given that we observe complete melting, and the potential is trained exclusively on distorted solid structures.

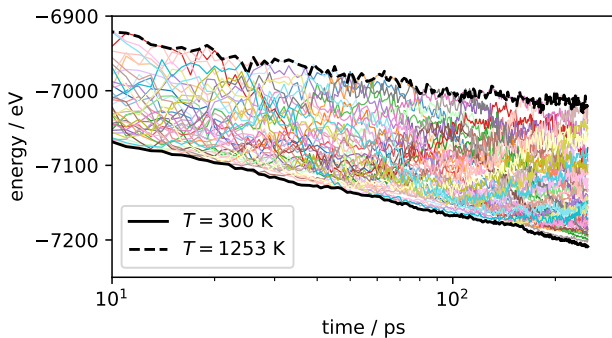


Figure 8. Trajectories of the potential energy for the 40 replicas used in one of the REMD simulations of a 864-atoms box of the HEA_{all}. Each color corresponds to a different initial configuration, that goes through cycles of heating and cooling due to REMD exchanges, accelerating the equilibration of the simulation at each temperature. The collection of trajectory segments corresponding to the extremal temperatures $T = 300$ K and $T = 1253$ K are highlighted with thicker, black lines. The logarithmic time scale refers to the MD integration time, but should not be interpreted as physical time given the presence of MC steps and replica exchange moves.

VI. TEMPERATURE-DEPENDENT SEGREGATION IN A CANTOR-STYLE ALLOY

In a seminal experiment, Cantor et al.² investigated the development of microstructure during the solidification of equimolar mixtures of 16 and 20 elements. We aim to perform a similar experiment in a computational setting, assessing the propensity of different elements to pair together or segregate, while covering the full component palette allowed by our model. This poses considerable challenges beyond the chemical complexity: kinetic trapping plays an important role in the physics of HEAs, and simulating vacancy-assisted atom diffusion requires time scales that are unattainable in brute-force atomistic modeling. In order to accelerate sampling and achieve (partial) equilibration, we run replica exchange simulations combining molecular dynamics and atom swap moves (REMD/MC), as described in Section III D.

Fig. 8 shows a representative trajectory for a 864-atoms cell, starting from *fcc* configurations, and including equimolar composition of all 25 elements (a composition we will refer to as HEA_{all}). The slow, logarithmic relaxation of the low-temperature replica is indicative of the glassy dynamics of the system, which does not equilibrate completely even after millions of MD/MC steps (see the Supplemental Material¹⁰³). For this reason, we perform multiple independent (and longer) simulations with a smaller box size (see the Supplemental Material¹⁰³). The qualitative observations on the local ordering are robust, even though the precise arrangement of atoms in the low-temperature regime, as measured by the element-resolved pair correlation functions, differ noticeably between trajectories.

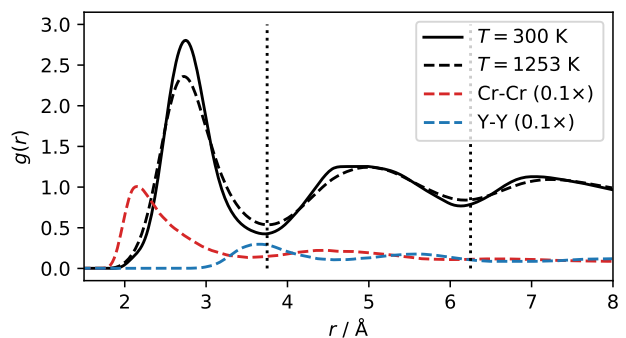


Figure 9. Pair correlation functions computed on a the $T = 300$ K (full) and $T = 1253$ K (dashed lines) replicas of a HEA_{all} box. Black lines correspond to the unresolved pair correlation, while red (Cr-Cr) and blue (Y-Y) lines provide representative examples of pair correlations resolved by species. The vertical dotted lines indicate the regions used in the definition of the pair ordering.

A. Relative pair probabilities for the HEA_{all} alloy

The pair correlation functions (Fig. 9) display broad, liquid-like peaks at both the highest and the lowest temperature we considered. In fact, simulations show little diffusion (except for some occasional bursts of activity at the high end of the temperature range) and the system can be characterized as an amorphous (or nano-crystalline) solid. The broadening of the peaks can be at least in part attributed to the diversity of pair distances between atomic species: some, like Cr-Cr, peak at distances as short as 2 Å, others, such as Y-Y, peak at about 3.7 Å. Note that typical distances in same-element pairs do not always match those found in the pure solid, underscoring the fact that the HEA25-4-NN can capture the effects arising from the heterogeneous chemical environments found in this alloy. For this reason, and given the disordered structure that develops in the supercell, we analyze structural correlations using a coarse-grained definition in which the first coordination shell extends up to a distance $r = 3.75$ Å, the second up to $r = 6.25$ Å and the third up to $r = 8$ Å, which is the largest distance we consider given the size of the box. We then define a variation on a theme of the short-range order parameter⁸⁴, which we dub the relative pair probability (RPP)

$$\text{RPP}_{\Delta r}(A, B) = \frac{p_{\Delta r}(A, B)}{p_{\Delta r}(\star, \star)} \frac{\rho^2}{\rho_A \rho_B} \quad (9)$$

which computes the number of pairs between species A and B that occur within a range Δr of distances, divided by the number of all pairs found in that same region, and normalized by the number density of the two species, $\rho_{A,B}$ and the overall number density ρ . $\text{RPP} = 1$ indicates that the two species are as likely to be found within a given separation range than any atom pair. $\text{RPP} > 1$ (< 1) indicate that they are more (less) likely to be found in that distance range.

Qualitatively, the value of the RPP in the first coordination shell is indicative of the propensity of two elements to cluster together or to separate from each other. However, the values cannot be interpreted in isolation, without considering the overall setup of the simulation: the finite size of the supercell, the imperfect equilibration, and the many-body interactions between all 25 species mean that the strong affinity between Y and Au, or the poor compatibility of Mn and Pd, do not necessarily imply the same quantitative effect when considered as part of a different overall composition. Fig. 10 shows a heat-map representation of $\text{RPP}_{\Delta r}(A, B)$ for the HEA_{all} at 300 K and 1253 K, and for the three regions indicated in Fig. 9. A few qualitative observations can be made. First, in our simulations HEA_{all} evolves to be far from random. Certain atom pairs have a strong tendency to associate or separate at low temperature, and the high-temperature samples (which are well equilibrated) show similar, even though less pronounced, trends. This correspondence is interesting, as it suggests one may use

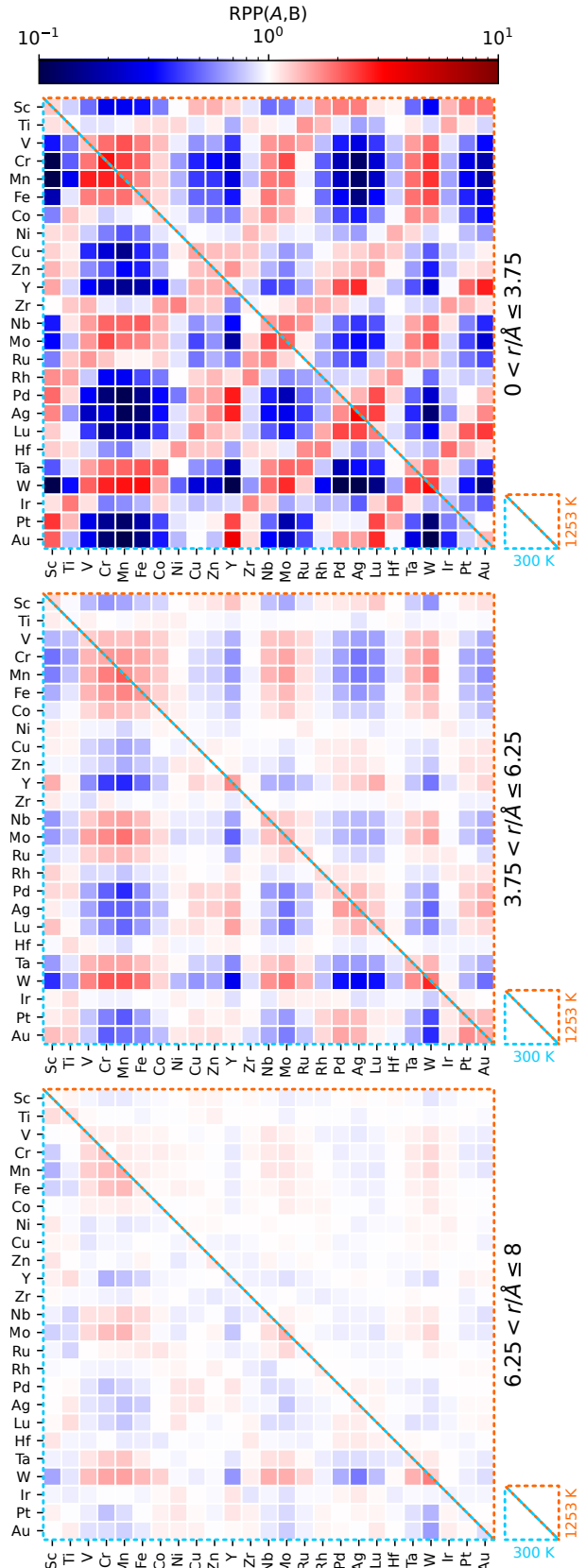


Figure 10. A plot of the relative pair probability for all atom pairs and the three regions corresponding to the first, second, and third peaks in the total pair correlation function (Fig. 9). Each plot is split across the diagonal, showing results for simulations of HEA_{all} at two temperatures, 300 K (lower-left corner) and 1253 K (top-right corner), averaged over the trajectories and discarding the first 100 ps (50'000 combined MD/MC steps).

high-temperature trajectories, that are easier to converge, to extract insights on the propensity of different species for association. The trends observed in the second and third region are very similar to those in the first-extended-neighbor shell, although progressively less pronounced: given the finite size of the simulation, and incomplete equilibration, the simulation does not generate clear-cut phase-separated regions.

Considering the RPP along the elements, one can observe a clear periodicity in behavior. Sc, Y, Hf, as well as the noble metals, Cu and Zn, tend to separate from V, Cr, Mn, Fe, which on the other hand have a tendency to cluster together, and also have positive associations to their heavier counterparts Nb, Mo, Ta, W. On the other hand, Sc, Y and (to a lesser degree) Hf associate strongly with noble metals, Cu, and Zn. The noble metals, Cu and Zn also tend to cluster together. Ti, Co, Ni, Zr, Ru, Ir have less clear-cut associations, and are closer to having a random distribution throughout the box. Another way of looking at the association plots in Fig. 10 is to check for consistency with known high-entropy alloys. The Cr-Mn-Fe-Co-Ni system is one of the prototypical sets of HEA formers, and indeed we observe strong mutual association tendency between Cr-Mn-Fe in the first shell, and also with Co and Ni in the second extended shell. Second-shell mutual association is also observed for noble-metal based compositions such as Ni-Cu-Pd-Pt-Au. Let us reiterate that strong mutual association for a group of elements in the HEA_{all} runs is a necessary, but not sufficient, conditions for that group of elements to be good HEA-forming candidates. For instance, some elements may have a strong tendency to form ordered intermetallics and might separate out of the mixture.

B. Data-driven Hume-Rothery rules

This analysis allows us to substantiate and quantify some of the empirical principles that are used in the design of HEAs, such as Hume-Rothery rules⁸⁵ that stipulate what elements can be substituted for each other with little effect on the HEA-forming propensity. We use the first-neighbor affinity of each species to all the other elements in the alloy to define a measure of dissimilarity as

$$d_{\text{RPP}}(A,B)^2 = \sum_X \left[\log_{10} \frac{\text{RPP}_1(A,X)}{\text{RPP}_1(B,X)} \right]^2, \quad (10)$$

that, roughly speaking, measures the relative strength of interactions between the two species and the other components. Two elements with a small distance are predicted to behave similarly, and vice versa. Fig. 11 paints a picture that is consistent with the observations we made on short and mid-range order between the elements in the HEA_{all}, and with much of the common wisdom in HEA research. We base this analysis on the high-temperature simulations to obtain a statistically-converged, and somewhat more nuanced,

definition, but the qualitative features of the map are similar to those one would obtain from the RPP computed at $T = 300$ K. Elements in the same group usually show strong similarity, but this is not always the case: for example, Cu is more similar to Zn than to Ag. The similarity matrix can also be converted to a 2D map, in which the Euclidean distance between elements approximates their RPP-based similarity (also shown in Fig. 11), which provides an easy-to-interpret visual representation of a set of data-driven rules to design HEAs. The element similarity that can be inferred from the RPP-based map differ – both quantitatively and conceptually – from that associated with the alchemical coupling matrix in Fig. 3. Whereas the weights are associated with the similarity in terms of the interatomic potential, the RPP similarity is a result of the collective behavior of the HEA_{all} at the prescribed thermodynamic conditions, not unlike the relation between a pair potential and the potential of mean force. This means, for example, that one could compute d_{RPP} for a different alloy composition (extending or refining the assessment of alloying behavior), from a different type of interatomic potential, or even from experimental data on partial structure factors.

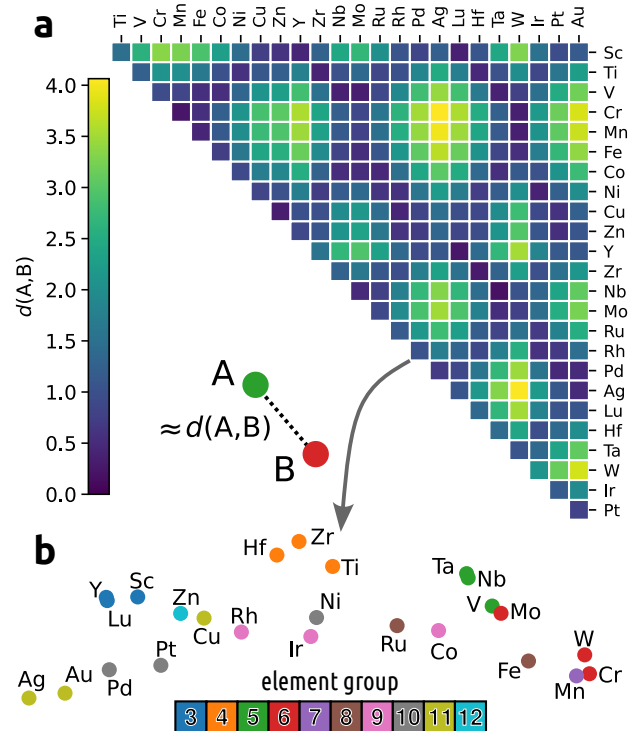


Figure 11. (a) Element similarity matrix based on the RPP distance (10) for the nearest-neighbor shell, in the HEA_{all} simulation at $T = 1253$ K. (b) The element similarity map (color-coded based on the group of the various transition metals) is built by applying metric multi-dimensional scaling to the distance matrix, and provides a visual aid to recognize groups of elements that have similar affinity patterns to the other d -block metals.

VII. BULK STRUCTURE OF HIGH-ENTROPY ALLOYS FOR CATALYSIS

Having demonstrated the accuracy of the HEA25-4-NN model, and used it to investigate the mutual affinity of the full set of 25 transition metals we considered in a Cantor-type computational experiment, we now turn our attention to a more focused study of three specific equimolar compositions. The first is the prototypical CoCrFeMnNi alloy, which was reported by Cantor et al.⁸⁶ in their seminal paper. This alloy is also known to be effective as a catalyst^{87–89}. Furthermore, we investigate CoCrFeMoNi^{11,90,91}, as an example of an alloy obtained by element substitution that has been broadly studied for its improved mechanical and tribological properties^{92,93}, as well as a catalyst of oxygen evolution reactions. We then consider IrPdPtRhRu^{21,94–97} as an example of an alloy based on sixth period elements that has recently received much attention as a catalyst for hydrogen evolution, and is often synthesized in the form of nanoparticles.

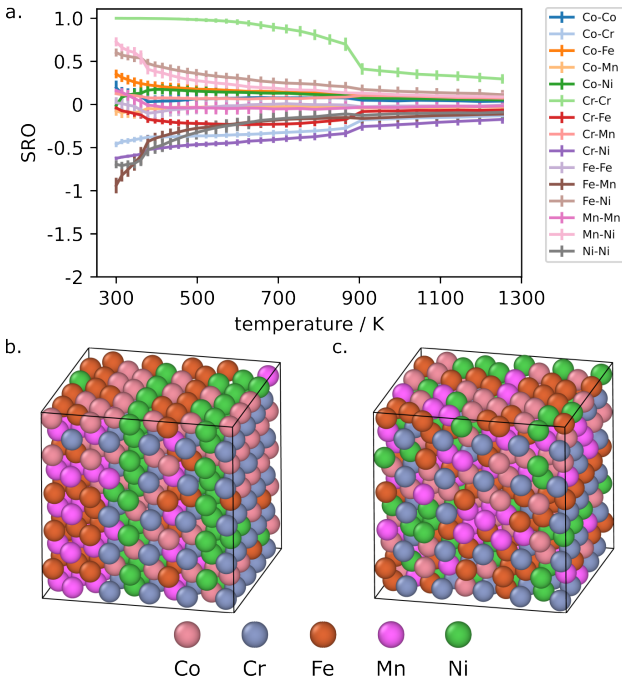


Figure 12. a. Cowley’s short-range (SRO) parameters for the first shell in CoCrFeMnNi HEA, shown for the 10 replicas between 300 and 1253 K, averaged over the last 1000 steps and two independent runs. At low temperatures, a tendency of Fe-Mn segregation can be seen. In contrast, Co is very well mixed. There are two phase transformations around 400 K and 900 K. The y-axis is adjusted to the example shown in Fig. 14 to facilitate comparison. b,c. snapshot from MC/MD simulations at $T = 300$ K and at $T = 720$ K, respectively. In the 300 K snapshot, two planes of Ni can be seen, while in the higher temperature snapshot, Cr order is evident (see the Supplemental Material¹⁰³).

To model the alloys, we used *fcc* lattices with 500 atoms per cell ($5 \times 5 \times 5$ super cell). We ran two independent REMD/MC runs according to Section III D

with a timestep of 2 fs and 32 temperature replicas, logarithmically spaced between 300 K and 1253 K. We discard the first 100ps for equilibration. Given that all these alloys maintain a regular *fcc* structure throughout the simulation, we analyze their structure in terms of Cowley’s short-range order⁸⁴ (SRO) which is commonly used in the study of HEAs and takes a value of zero when atoms are distributed fully randomly, becomes negative for pairs of atoms that tend to cluster together, and tends to one when two atom types never appear as first neighbors. In the Supplemental Material¹⁰³ we also report an analysis in terms of the RPP that incorporates second-neighbor and long-range correlations. In interpreting these results, one should consider similar considerations to those we discussed for the HEA_{all} simulations: (1) the SRO (and the RPP) are only meaningful for homogeneous phases, and in case of phase separation the values computed for the whole cell serve only to signal the occurrence of a phase transition; (2) a combination of finite-size effects and glassy behavior can hinder reaching full equilibrium in simulations; (3) since they allow for atom exchanges, our simulations cannot give quantitative indications on whether different phases are only metastable, nor on the kinetics of diffusion processes that are required for precipitation.

We start by analyzing the Cantor alloy CoCrFeMnNi. The SRO computed at different temperatures (Fig. 12a, plotted for all element combinations) indicate the presence of at least two phase transitions. The high-temperature phase is homogeneous and disordered, but shows substantial ordering, particularly for the Cr-Cr pair. At approximately 900 K we observe a first transition, that is associated with the ordering of Cr atoms. The SRO for the Cr-Cr pair tends to one (as there are almost no first-neighbor chromium atoms) but the RPP show a clear increase of second-neighbor Cr-Cr pairs, consistent with the formation of a simple cubic sublattice. The other elements remain relatively disordered, and no discontinuous behavior is observed in the SRO. As the temperature is reduced further, a second transition occurs around 400 K. The most prominent structural transformation is the formation of (100) Ni planes, separated by (Co,Fe,Mn)-rich regions forming a layered superstructure. Fig. 12b,c show snapshots of the simulations at 300 K and 720 K, that give an idea of the partially-ordered structure of the two phases.

Substituting Mn with Mo changes the segregation behavior significantly (Fig. 13a): the SRO parameters are generally smaller, with the largest segregation tendency found for the Mo-Ni atom pair. The tendency of Cr to form a cubic sublattice is less pronounced than CoCrFeMnNi, and one only sees the increase of SRO parameters at around 500 K. At low temperature, (100) planes of Ni form that are very similar to those observed in the Mn-based counterpart (Fig. 13b,c), that are separated by (Co,Fe,Mo)-rich regions. Given the sizable energy errors of the ML models, as well as those of the underlying DFT reference, one should not overinterpret the details of the struc-

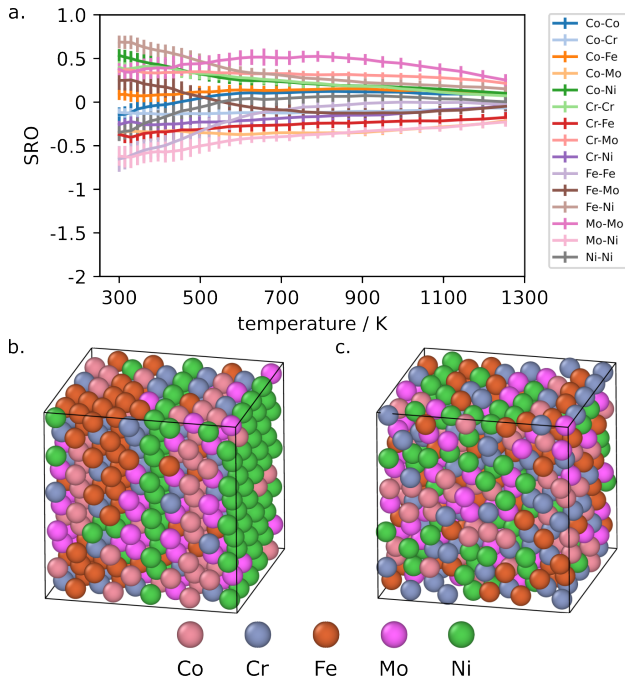


Figure 13. a. Cowley’s short-range (SRO) parameters for the first shell in CoCrFeMoNi HEA, shown for the 10 replicas between 300 and 1253 K, averaged over the last 1000 steps and two independent runs. Good mixing of atomic species can be assumed due to the small values of SRO parameters. The y-axis is adjusted to the example shown in Fig. 14 to facilitate comparison. b,c. snapshot from MC/MD simulations at $T = 300$ K and at $T = 1253$ K, respectively. In the 300 K snapshot, two planes of Ni can be seen.

tures we observe. Even if *fcc* CoCrFeMnNi is paramagnetic, neglect of magnetism in the presence of several elements which form ferromagnetic phases is worrisome (see e.g. Ref. 98 for a thorough discussion of magnetism in CoCrFeMnNi and CoCrFeMoNi). That said, our observations provide strong indications of the tendency to form partly ordered phases with a complex structure, which, together with the low vacancy-mediated diffusivity,⁹⁹ help explain the observed stability of HEAs that contain (Co,Fe,Cr,Ni). A tendency to develop short-range ordering is consistent with previous simulations in other classes of HEAs,¹⁰⁰ and with observation of phase separation in equimolar CoCrFeMnNi in high-mobility environments such as grain boundaries¹⁰¹ or under deformation¹⁰².

While the leading effect in CoCrFeMnNi and CoCrFeMoNi is the appearance of partial ordering at low temperatures, in the case of IrPdPtRhRu we observe clear-cut phase separation between a (Pd,Pt) and a (Ru,Ir,Rh) phase, with Rh accumulating preferentially at the interface between the two phases (see Fig. 14b,c). The strong tendency to segregate is already evident in the high-temperature regime, where the system is visually well-mixed, but with large SRO parameters. This is in contrast to the experimental observation that this HEA forms a complex solid solution with random atom distribution^{21,96}. As shown in

the Supplemental Material¹⁰³, the large enthalpic gain arising from demixing is not an artefact of HEA25-4-NN, and the ML error on the free-energy change upon ordering is of the order of 3 meV/atom. These observations suggest that kinetic trapping, or finite-size effects associated with the synthesis in the form of nanoparticles, might be key to stabilize a homogeneous phase.

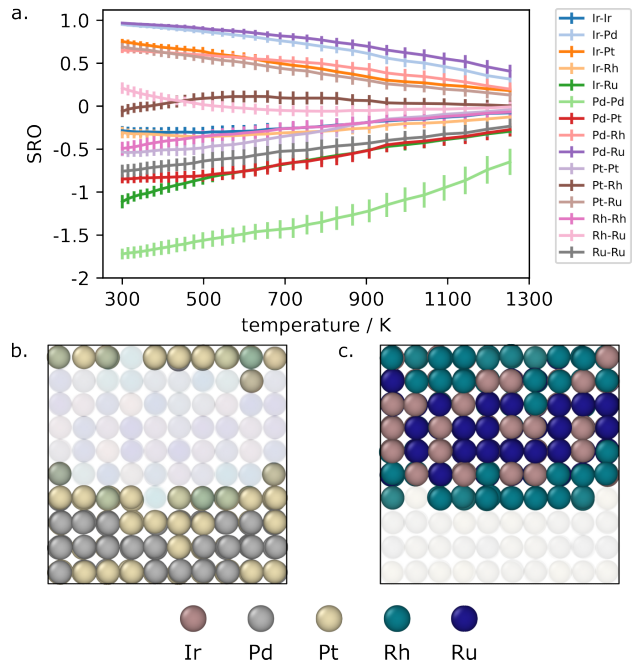


Figure 14. a. Cowley’s short-range parameters for the first shell in IrPdPtRhRu HEA, shown for the 10 replicas between 500 and 933 K, averaged over the last 1000 frames and with an error estimation from independent repetition runs. The most pronounced local order can be seen for the Pd-Pd atom pair (light green line, mathematically smallest SRO). Demonstration of the phase segregation tendency by highlighting the b. PdPt and c. IrRhRu atoms in an MC/MD snapshot.

VIII. CONCLUSIONS

The notion that different chemical elements may behave similarly when combined with others is one of the founding principles of chemistry, and is often used as guidance in the design of new materials. We build a ML framework that incorporates this notion in the form of a linear compression of chemical space, and succeed in training a potential that can describe with semi-quantitative accuracy bulk phases of arbitrary combinations of 25 *d*-block elements. The physically-motivated, intuitive functional form of the contraction allows us to analyze critically the model performance, allowing us to show that 3-4 dimensions suffice to capture the diversity of behavior of the transition metal block. The optimized values of the combination weights reveal relationships between the elements that match their arrangement in the periodic table, to

the point where we show it is possible to “fill in the blanks” for missing elements, with only a moderate loss of accuracy.

We use the potential to run an ambitious computational experiment, in which we attempt to equilibrate an equimolar mixture of all 25 elements, resulting in the formation of a disordered structure with strong element segregation. The affinity between elements is consistent with several known high-entropy alloys, and allows us to define a data-driven version of the Hume-Rothery rules, that could be further adapted to subsets of elements that are relevant for a given application. We also investigate in detail three specific compositions - the archetypal Cantor alloy CoCrFeMnNi, which we observe to be undergo a sequence of transitions towards complex ordered phases as the temperature is lowered; that arising from the Mn→Mo substitution, which also leads to similar, although less pronounced, ordering; the noble metal alloy PdPtIrRuRh, that shows a strong tendency to decompose into PdPt and IrRhRu phases.

We are only scratching the surface of what can be achieved within this framework. Extending the dataset to an even more diverse palette of compounds, and to structures that include molten and defective configurations, is an obvious direction for further improvements. A more systematic exploration of the design space of chemical compression is another promising research direction, even though doing so may sacrifice, at least in part, the interpretability of the linear contraction we use here. On a more application-focused front, a systematic study of the stability of 4 and 5-element HEAs along the same lines of the simulations of those which we present here, based on the current HEA25-4-NN model, will provide much-needed insights into the stability range of multi-principal-component alloys, guiding synthetic efforts towards compositions that are stable towards phase separation.

DATA AVAILABILITY

All data and code used to train the HEA25-4-NN model, as well as the fitted parameters and code to run the simulations discussed in this work is available in the Supplemental Material¹⁰³ or from publicly-accessible repositories (<https://github.com/Luthaf/alchemical-learning> and <https://archive.materialscloud.org/record/2023.57>).

ACKNOWLEDGEMENTS

We thank William Curtin and Binglun Yin for sharing a dataset we used in the early developments of this work, and Anirudh Natarajan for discussion on an early version of the manuscript. MC and NL acknowledge support from the NCCR MARVEL, funded by the Swiss National Science Foundation (grant number 182892) and from an Indus-

trial Grant from BASF. GF acknowledges support by the Swiss Platform for Advanced Scientific Computing (PASC). Electronic-structure calculations were performed within the scope of a CSCS project (ID: s1092).

REFERENCES

- J.-W. Yeh, S.-K. Chen, S.-J. Lin, J.-Y. Gan, T.-S. Chin, T.-T. Shun, C.-H. Tsau, and S.-Y. Chang, *Adv. Eng. Mater.* **6**, 299 (2004).
- B. Cantor, I. Chang, P. Knight, and A. Vincent, *Materials Science and Engineering: A* **375–377**, 213 (2004).
- B. Cantor, *Progress in Materials Science* **120**, 100754 (2021).
- E. George, W. Curtin, and C. Tasan, *Acta Materialia* **188**, 435 (2020).
- W. Li, D. Xie, D. Li, Y. Zhang, Y. Gao, and P. K. Liaw, *Progress in Materials Science* **118**, 100777 (2021).
- Y. Sun and S. Dai, *Science Advances* **7** (2021), 10.1126/sciadv.abg1600.
- B. Wang, Y. Yao, X. Yu, C. Wang, C. Wu, and Z. Zou, *Journal of Materials Chemistry A* **9**, 19410 (2021).
- W.-Y. Huo, S.-Q. Wang, W.-H. Zhu, Z.-L. Zhang, F. Fang, Z.-H. Xie, and J.-Q. Jiang, *Tungsten* **3**, 161 (2021).
- Y. Zhang, D. Wang, and S. Wang, *Small* **18**, 2104339 (2021).
- X. Huo, H. Yu, B. Xing, X. Zuo, and N. Zhang, *The Chemical Record* (2022), 10.1002/tcr.202200175.
- G. Zhang, K. Ming, J. Kang, Q. Huang, Z. Zhang, X. Zheng, and X. Bi, *Electrochimica Acta* **279**, 19 (2018).
- M. Bondesgaard, N. L. N. Broge, A. Mamakhel, M. Bremholm, and B. B. Iversen, *Advanced Functional Materials* **29**, 1905933 (2019).
- M. W. Glasscott, A. D. Pendergast, S. Goines, A. R. Bishop, A. T. Hoang, C. Renault, and J. E. Dick, *Nature Communications* **10** (2019), 10.1038/s41467-019-10303-z.
- Z. Jin, J. Lv, H. Jia, W. Liu, H. Li, Z. Chen, X. Lin, G. Xie, X. Liu, S. Sun, and H.-J. Qiu, *Small* **15**, 1904180 (2019).
- S. D. Lacey, Q. Dong, Z. Huang, J. Luo, H. Xie, Z. Lin, D. J. Kirsch, V. Vattipalli, C. Povinelli, W. Fan, R. Shahbazian-Yassar, D. Wang, and L. Hu, *Nano Letters* **19**, 5149 (2019).
- M. Liu, Z. Zhang, F. Okejiri, S. Yang, S. Zhou, and S. Dai, *Advanced Materials Interfaces* **6**, 1900015 (2019).
- H.-J. Qiu, G. Fang, J. Gao, Y. Wen, J. Lv, H. Li, G. Xie, X. Liu, and S. Sun, *ACS Materials Letters* **1**, 526 (2019).
- H.-J. Qiu, G. Fang, Y. Wen, P. Liu, G. Xie, X. Liu, and S. Sun, *Journal of Materials Chemistry A* **7**, 6499 (2019).
- S. Gao, S. Hao, Z. Huang, Y. Yuan, S. Han, L. Lei, X. Zhang, R. Shahbazian-Yassar, and J. Lu, *Nature Communications* **11** (2020), 10.1038/s41467-020-15934-1.
- K. Huang, B. Zhang, J. Wu, T. Zhang, D. Peng, X. Cao, Z. Zhang, Z. Li, and Y. Huang, *Journal of Materials Chemistry A* **8**, 11938 (2020).
- D. Wu, K. Kusada, T. Yamamoto, T. Toriyama, S. Matsumura, I. Gueye, O. Seo, J. Kim, S. Hiroi, O. Sakata, S. Kawaguchi, Y. Kubota, and H. Kitagawa, *Chemical Science* **11**, 12731 (2020).
- X. Chen, C. Si, Y. Gao, J. Frenzel, J. Sun, G. Eggeler, and Z. Zhang, *Journal of Power Sources* **273**, 324 (2015).
- T. Löffler, H. Meyer, A. Savan, P. Wilde, A. G. Manjón, Y.-T. Chen, E. Ventosa, C. Scheu, A. Ludwig, and W. Schuhmann, *Advanced Energy Materials* **8**, 1802269 (2018).
- S. Li, X. Tang, H. Jia, H. Li, G. Xie, X. Liu, X. Lin, and H.-J. Qiu, *Journal of Catalysis* **383**, 164 (2020).
- J. Barranco and A. Pierna, *Journal of Non-Crystalline Solids* **354**, 5153 (2008).
- C.-F. Tsai, K.-Y. Yeh, P.-W. Wu, Y.-F. Hsieh, and P. Lin, *Journal of Alloys and Compounds* **478**, 868 (2009).
- A.-L. Wang, H.-C. Wan, H. Xu, Y.-X. Tong, and G.-R. Li, *Electrochimica Acta* **127**, 448 (2014).
- K. V. Yuseenko, S. Riva, P. A. Carvalho, M. V. Yuseenko, S. Arnaboldi, A. S. Sukhikh, M. Hanfland, and S. A.

- Gromilov, *Scripta Materialia* **138**, 22 (2017).
- ²⁹J.-W. Yeh, *JOM* **65**, 1759 (2013).
- ³⁰E. J. Pickering and N. G. Jones, *International Materials Reviews* **61**, 183 (2016).
- ³¹J. Sanchez, F. Ducastelle, and D. Gratias, *Physica A: Statistical Mechanics and its Applications* **128**, 334 (1984).
- ³²C. M. Nataraj, A. van de Walle, and A. Samanta, *J. Phase Equilib. Diffus.* **42**, 571 (2021).
- ³³Y. Rao and W. Curtin, *Acta Materialia* **226**, 117621 (2022).
- ³⁴D. Ma, B. Grabowski, F. Körmann, J. Neugebauer, and D. Raabe, *Acta Materialia* **100**, 90 (2015).
- ³⁵D. Farkas and A. Caro, *Journal of Materials Research* **33**, 3218 (2018).
- ³⁶J. Byggmästar, K. Nordlund, and F. Djurabekova, *Physical Review B* **104** (2021), 10.1103/physrevb.104.104101.
- ³⁷C. W. Rosenbrock, K. Gubaev, A. V. Shapeev, L. B. Pártay, N. Bernstein, G. Csányi, and G. L. W. Hart, *npj Comput Mater* **7**, 24 (2021).
- ³⁸Y. Zhou, P. Srinivasan, F. Körmann, B. Grabowski, R. Smith, P. Goddard, and A. I. Duff, *Phys. Rev. B* **105**, 214302 (2022).
- ³⁹M. J. Willatt, F. Musil, and M. Ceriotti, *Phys. Chem. Chem. Phys.* **20**, 29661 (2018).
- ⁴⁰M. J. Willatt, F. Musil, and M. Ceriotti, *J. Chem. Phys.* **150**, 154110 (2019).
- ⁴¹A. V. Shapeev, *Multiscale Model. Simul.* **14**, 1153 (2016).
- ⁴²R. Drautz, *Phys. Rev. B* **99**, 014104 (2019).
- ⁴³F. Musil, A. Grisafi, A. P. Bartók, C. Ortner, G. Csányi, and M. Ceriotti, *Chem. Rev.* **121**, 9759 (2021).
- ⁴⁴A. P. Bartók, R. Kondor, and G. Csányi, *Phys. Rev. B* **87**, 184115 (2013).
- ⁴⁵J. Behler, *The Journal of Chemical Physics* **134**, 074106 (2011).
- ⁴⁶G. C. Schatz, *J. Phys. Chem. Lett.* **10**, 5956 (2019).
- ⁴⁷N. Artrith, A. Urban, and G. Ceder, *Phys. Rev. B* **96**, 014112 (2017).
- ⁴⁸M. Gastegger, L. Schwiedrzik, M. Bittermann, F. Berzsenyi, and P. Marquetand, *J. Chem. Phys.* **148**, 241709 (2018).
- ⁴⁹J. P. Darby, J. R. Kermode, and G. Csányi, *npj Comput Mater* **8**, 166 (2022).
- ⁵⁰A. Goscinski, F. Musil, S. Pozdnyakov, J. Nigam, and M. Ceriotti, *J. Chem. Phys.* **155**, 104106 (2021).
- ⁵¹J. Nigam, S. Pozdnyakov, and M. Ceriotti, *J. Chem. Phys.* **153**, 121101 (2020).
- ⁵²A. Paszke, S. Gross, F. Massa, A. Lerer, J. Bradbury, G. Chanan, T. Killeen, Z. Lin, N. Gimeshin, L. Antiga, A. Desmaison, A. Kopf, E. Yang, Z. DeVito, M. Raison, A. Tejani, S. Chilamkurthy, B. Steiner, L. Fang, J. Bai, and S. Chintala, in *Advances in Neural Information Processing Systems 32*, edited by H. Wallach, H. Larochelle, A. Beygelzimer, F. dAlché-Buc, E. Fox, and R. Garnett (Curran Associates, Inc., 2019) pp. 8024–8035.
- ⁵³G. Kresse and J. Furthmüller, *Phys. Rev. B* **54**, 11169 (1996).
- ⁵⁴G. I. Csonka, J. P. Perdew, A. Ruzsinszky, P. H. Philipsen, S. Lebègue, J. Paier, O. A. Vydrov, and J. G. Ángyán, *Physical Review B* **79**, 155107 (2009).
- ⁵⁵G. Kresse and D. Joubert, *Physical review b* **59**, 1758 (1999).
- ⁵⁶H. J. Monkhorst and J. D. Pack, *Phys. Rev. B* **13**, 5188 (1976).
- ⁵⁷I. Novikov, B. Grabowski, F. Körmann, and A. Shapeev, *npj Comput Mater* **8**, 13 (2022).
- ⁵⁸C. S. Wang, R. E. Prange, and V. Korenman, *Phys. Rev. B* **25**, 5766 (1982).
- ⁵⁹J. Kubler, K. H. Hock, J. Sticht, and A. R. Williams, *J. Phys. F: Met. Phys.* **18**, 469 (1988).
- ⁶⁰H. J. Kulik, M. Cococcioni, D. A. Scherlis, and N. Marzari, *Phys. Rev. Lett.* **97**, 103001 (2006).
- ⁶¹Z. Li, A. Ludwig, A. Savan, H. Springer, and D. Raabe, *Journal of Materials Research* **33**, 3156 (2018).
- ⁶²G. Imbalzano, A. Anelli, D. Giofré, S. Klees, J. Behler, and M. Ceriotti, *J. Chem. Phys.* **148**, 241730 (2018).
- ⁶³S. Haykin, *Neural Networks: A Comprehensive Foundation* (Prentice Hall PTR, 1994).
- ⁶⁴F. Musil, M. Veit, A. Goscinski, G. Fraux, M. J. Willatt, M. Stricker, and M. Ceriotti, *J. Chem. Phys.* **154**, 114109 (2021).
- ⁶⁵J. Behler and M. Parrinello, *Phys. Rev. Lett.* **98**, 146401 (2007).
- ⁶⁶D. C. Liu and J. Nocedal, *Mathematical Programming* **45**, 503 (1989).
- ⁶⁷H. C. Andersen, *J. Chem. Phys.* **72**, 2384 (1980).
- ⁶⁸G. Bussi, T. Zykova-Timan, and M. Parrinello, *J. Chem. Phys.* **130**, 074101 (2009).
- ⁶⁹M. Ceriotti, G. Bussi, and M. Parrinello, *J. Chem. Theory Comput.* **6**, 1170 (2010).
- ⁷⁰G. Bussi, D. Donadio, and M. Parrinello, *J. Chem. Phys.* **126**, 14101 (2007).
- ⁷¹N. Metropolis, A. W. Rosenbluth, M. N. Rosenbluth, A. H. Teller, and E. Teller, *J. Chem. Phys.* **21**, 1087 (1953).
- ⁷²D. J. Earl and M. W. Deem, *Phys. Chem. Chem. Phys.* **7**, 3910 (2005).
- ⁷³V. Kapil, M. Rossi, O. Marsalek, R. Petraglia, Y. Litman, T. Spura, B. Cheng, A. Cuzzocrea, R. H. Meißner, D. M. Wilkins, B. A. Helfrecht, P. Juda, S. P. Bienvenue, W. Fang, J. Kessler, I. Poltavsky, S. Vandenbrande, J. Wieme, C. Corminboeuf, T. D. Kühne, D. E. Manolopoulos, T. E. Markland, J. O. Richardson, A. Tkatchenko, G. A. Tribello, V. Van Speybroeck, and M. Ceriotti, *Comput. Phys. Commun.* **236**, 214 (2019).
- ⁷⁴G. Imbalzano and M. Ceriotti, *Phys. Rev. Materials* **5**, 063804 (2021).
- ⁷⁵R. Petraglia, A. Nicolai, M. D. Wodrich, M. Ceriotti, and C. Corminboeuf, *J. Comput. Chem.* **37**, 83 (2016).
- ⁷⁶F. A. Faber, A. Lindmaa, O. A. Von Lilienfeld, and R. Armiento, *Phys. Rev. Lett.* **117**, 135502 (2016).
- ⁷⁷V. L. Deringer and G. Csányi, *Phys. Rev. B* **95**, 094203 (2017).
- ⁷⁸V. L. Deringer, A. P. Bartók, N. Bernstein, D. M. Wilkins, M. Ceriotti, and G. Csányi, *Chem. Rev.* **121**, 10073 (2021).
- ⁷⁹G. T. Seaborg, *Plutonium: The Ornerly Element* (1964).
- ⁸⁰D. Sheppard, G. Henkelman, and O. A. von Lilienfeld, *The Journal of Chemical Physics* **133**, 084104 (2010).
- ⁸¹L. Bellaiche and D. Vanderbilt, *Phys. Rev. B* **61**, 7877 (2000).
- ⁸²C. Chen and S. P. Ong, “A universal graph deep learning interatomic potential for the periodic table,” (2022).
- ⁸³A. Jain, S. P. Ong, G. Hautier, W. Chen, W. D. Richards, S. Dacek, S. Cholia, D. Gunter, D. Skinner, G. Ceder, and K. A. Persson, *APL Materials* **1**, 011002 (2013).
- ⁸⁴J. M. Cowley, *Physical Review* **77**, 669 (1950).
- ⁸⁵U. Mizutani, *MRS Bulletin* **37**, 169–169 (2012).
- ⁸⁶B. Cantor, I. Chang, P. Knight, and A. Vincent, *Materials Science and Engineering: A* **375-377**, 213 (2004).
- ⁸⁷F. Waag, Y. Li, A. R. Zieffuß, E. Bertin, M. Kamp, V. Duppel, G. Marzun, L. Kienle, S. Barcikowski, and B. Gökce, *RSC Advances* **9**, 18547 (2019).
- ⁸⁸H. Peng, Y. Xie, Z. Xie, Y. Wu, W. Zhu, S. Liang, and L. Wang, *Journal of Materials Chemistry A* **8**, 18318 (2020).
- ⁸⁹R. He, L. Yang, Y. Zhang, X. Wang, S. Lee, T. Zhang, L. Li, Z. Liang, J. Chen, J. Li, A. O. Moghaddam, J. Llorca, M. Ibanez, J. Arbiol, Y. Xu, and andreu cabot, *SSRN Electronic Journal* (2022), 10.2139/ssrn.4289857.
- ⁹⁰J. Tang, J. Xu, Z. Ye, X. Li, and J. Luo, *Journal of Materials Science and Technology* **79**, 171 (2021).
- ⁹¹S. Schumacher, S. Baha, A. Savan, C. Andronescu, and A. Ludwig, *Journal of Materials Chemistry A* **10**, 9981 (2022).
- ⁹²G. Cui, B. Han, Y. Yang, Y. Wang, and H. Chunyang, *Journal of Materials Research and Technology* **9**, 2598 (2020).
- ⁹³Z. Wang, J. Jin, G.-H. Zhang, X.-H. Fan, and L. Zhang, *Corrosion Science* **208**, 110661 (2022).
- ⁹⁴T. A. Batchelor, J. K. Pedersen, S. H. Winther, I. E. Castelli, K. W. Jacobsen, and J. Rossmeisl, *Joule* **3**, 834 (2019).

- ⁹⁵N. L. N. Broge, M. Bondesgaard, F. Søndergaard-Pedersen, M. Roelsgaard, and B. B. Iversen, *Angewandte Chemie* **132**, 22104 (2020).
- ⁹⁶J. K. Pedersen, C. M. Clausen, O. A. Krysiak, B. Xiao, T. A. A. Batchelor, T. Löffler, V. A. Mints, L. Banko, M. Arenz, A. Savan, W. Schuhmann, A. Ludwig, and J. Rossmeisl, *Angewandte Chemie* **133**, 24346 (2021).
- ⁹⁷G. Lee, N.-A. Nguyen, V.-T. Nguyen, L. L. Larina, E. Chulunbat, E. Park, J. Kim, H.-S. Choi, and M. Keidar, *Journal of Solid State Chemistry* **314**, 123388 (2022).
- ⁹⁸J. Šebesta, K. Carva, and D. Legut, *Phys. Rev. Materials* **3**, 124410 (2019).
- ⁹⁹K.-Y. Tsai, M.-H. Tsai, and J.-W. Yeh, *Acta Materialia* **61**, 4887 (2013).
- ¹⁰⁰S. Chen, Z. H. Aitken, S. Pattamatta, Z. Wu, Z. G. Yu, D. J. Srolovitz, P. K. Liaw, and Y.-W. Zhang, *Nat Commun* **12**, 4953 (2021).
- ¹⁰¹M. Glienke, M. Vaidya, K. Gururaj, L. Daum, B. Tas, L. Rogal, K. Pradeep, S. V. Divinski, and G. Wilde, *Acta Materialia* **195**, 304 (2020).
- ¹⁰²K. H. Lee, S.-K. Hong, and S. I. Hong, *Materialia* **8**, 100445 (2019).
- ¹⁰³See Supplemental Material for further details on the models, reference data and example inputs of simulations. .

Modeling high-entropy transition-metal alloys with alchemical compression

Supporting Materials

Nataliya Lopanitsyna,¹ Guillaume Fraux,¹ Maximilian A. Springer,² Sandip De,² and Michele Ceriotti¹

¹*Laboratory of Computational Science and Modeling, Institute of Materials, École Polytechnique Fédérale de Lausanne, 1015 Lausanne, Switzerland*

²*BASF SE, Carl-Bosch-Straße 38, 67056 Ludwigshafen, Germany*

I. COMPUTATIONAL DETAILS

A. Electronic structure details

All the reference energies and forces are computed using density-functional theory (DFT), as implemented in the VASP code¹, with the PBEsol exchange-correlation functional². The core electrons are treated implicitly using projector augmented wave (PAW) pseudopotentials³. We choose conservative values for the convergence parameters of the electronic structure calculation, setting the cutoff for the plane-waves expansion of the wavefunction to 550 eV, which is more than 50% larger than largest recommended value across all the elements we considered, and the Brillouin zone sampling uses a Γ centered Monkhorst-Pack scheme⁴ with an interval between k-points along reciprocal lattice vector $0.04 \pi \text{ \AA}^{-1}$. To support the choice of k-point density, we show below the convergence of the cohesive energy difference levelled against corresponding the most converged calculation (k-point density of $0.025 \pi \text{ \AA}^{-1}$) for four representative structures from the dataset as a function of k-point grid density.

As we mentioned in the main text, all the calculations for the HEA25 dataset were performed with non-polarized DFT. We recalculated a small data set containing 944 FCC ideal crystal structures in order to assess the effects of selecting a different level of theory. The discrepancy on energies and forces amounts to 7 meV/at. MAE, 14 meV/at. RMSE, and 38 meV/ \AA MAE, 91 meV/ \AA RMSE correspondingly, which is comparable with the accuracy of the ML model.

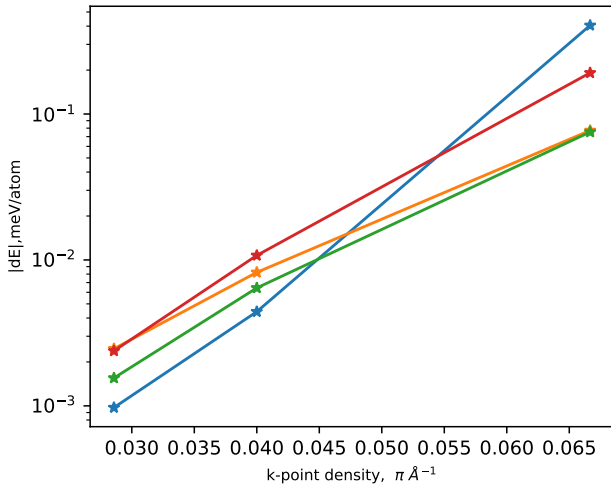


Figure S1. The convergence of the difference in cohesive energy relative to the most converged structure (k-point density of $0.025 \pi \text{ \AA}^{-1}$), for four representative structures in the data set.

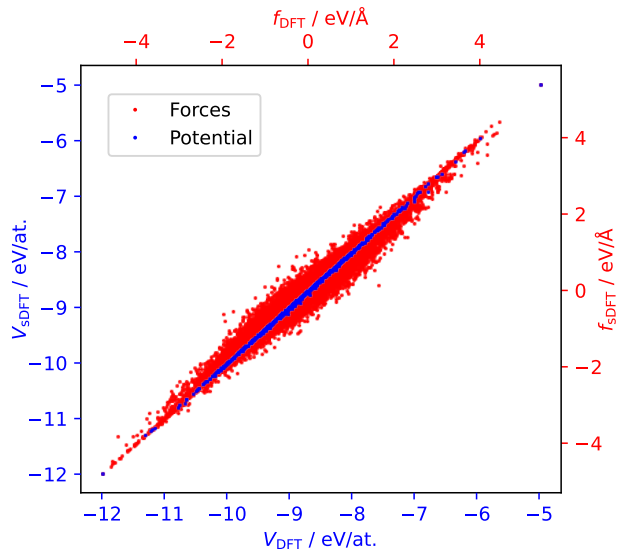


Figure S2. Parity plot between energies and forces computed with spin polarization (sDFT) and without (DFT, level of theory used in the article). The values were computed on a separate dataset of 944 structures. Energy error: 7 meV/at. MAE, 14 meV/at. RMSE, Force error: 38 meV/ \AA MAE, 91 meV/ \AA RMSE.

B. ML Details

In this section, we report the details of the HEA25-4-NN model. The final model HEA25-4-NN includes an atomic-energy baseline (25 weights), linear regression based on 2-body and 3-body correlation features (7500 and 1936 weights respectively), and a multi-layer perceptron with 80-nodes hidden layers (161521 weights, mostly associated with the initial linear layer that compresses the 2 and 3-body weights down to 80 channels). As the result of the alchemical compression with four pseudo-elements, the feature vector size decreases from the original 75625 to 1936. We use a training set containing energies from 25k structures (N_E) and forces from 2k structures (N_F) and a hold-out testing set containing 500 structures with energies and forces. The loss function is expressed as:

$$\mathcal{L} = \frac{1}{N_E} \sum_n^{N_E} (\hat{E}_n - E_n)^2 + \frac{C_F}{N_F} \sum_{i=1}^{N_F \cdot I_F} \sum_{\alpha=1}^3 (\hat{F}_{i,\alpha} - F_{i,\alpha})^2 + \lambda_1 \|w_1\| + \lambda_2 \|w_2\| + \lambda_3 \|w_3\| + \lambda_{NN} \sum \|w_{NN}\|, \quad (1)$$

where \hat{E}_n and E_n are predicted and reference energies, $\hat{F}_{i,\alpha}$ and $F_{i,\alpha}$ predicted and reference forces, I the total number of atoms for which forces are considered in training, C_F is a scaling factor set to 1e-3, $\lambda_{1,2,3,NN}$ (respectively $w_{1,2,3,NN}$) are the regularizers (respectively weight matrices) for the linear 1 (aeb), 2, 3-body, and NN models. These regularizers are set to 10^{-4} for $\lambda_{1,2,3}$ and 10^{-2} for λ_{NN} .

For two-body and three-body representations, we use GTO basis functions and radial scaling following Ref. 5. Table I presents the hyper-parameters used in the HEA25-4-NN. The model weights (best.torch) and its parameters (parameters.json) are provided in the Supplementary Materials.

	two-body	three-body
$\sigma_w/\text{\AA}$	0.25	0.3
$r_{cut}/\text{\AA}$	6.0	5.0
n_{alch}		4
n_{max}, l_{max}	12	8, 4*

Table I. Key hyper-parameters of the HEA25-4-NN model. Here σ_w is the Gaussian width, r_{cut} – the cutoff radius, n_{alch} – the number of alchemical channels, n_{max} and l_{max} – the number of radial and angular channels. For the three-body representation we used a different number of radial channels for every l . The complete set of parameters can be found in the parameters.json file, which is provided in the Supplementary Materials.

II. ALCHEMICAL CONTRACTION

A. Weight analysis

We continue the analysis of the alchemical compression by demonstrating the evolution of the alchemical weights matrix \mathbf{u}_{alch} during the optimization process (Fig. S3). Despite initializing the weights of \mathbf{u}_{alch} with physical priors - a singular value decomposition of a Gaussian similarity kernel based on electronegativity and atomic radius of the elements, as in Ref. 5 - one does not observe a clear arrangement of the elements according to their positions in the d block (Fig. S3, left panel). Some elements are projected in the vicinity of their conventional periodic table neighbours, while others such as Mn are grouped with dissimilar elements.

Conversely, the optimized weight for the HEA25-4-NN potential (Fig. S3, right panel, corresponding to the figure in the main text) are clearly laid out as in a distorted version of the transition metal block. This regular arrangement is obtained in both the HEA25-4-NN model and in the linear models, as shown in Fig. S4. With the exception of $\mathbf{n}_{\text{alch}} = 2$ (where the excessive compression leads to an irregular distribution) the optimized weight reflect the position of the elements in the periodic table. Furthermore, the comparison of the explained variance's plots for linear models (Fig. S5), confirms that for the optimized weights the first three components carry the most information about chemical diversity for the chosen set of elements.

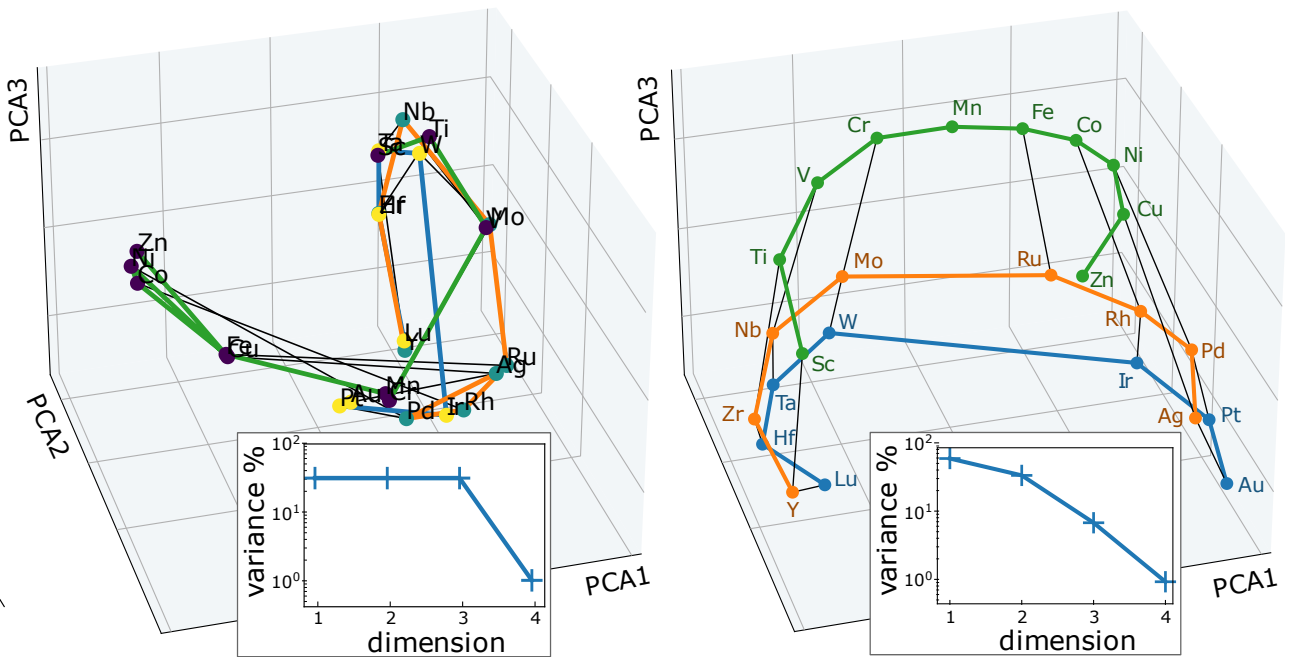


Figure S3. Top-3 principal components of the initial (left) and converged (right) alchemical weights matrix \mathbf{u}_{alch} for the HEA25-4-NN model. The periods are highlighted with orange, blue and green lines, and the columns are indicated by black thin lines. The insets show the decay of explained variance with number of alchemical channels

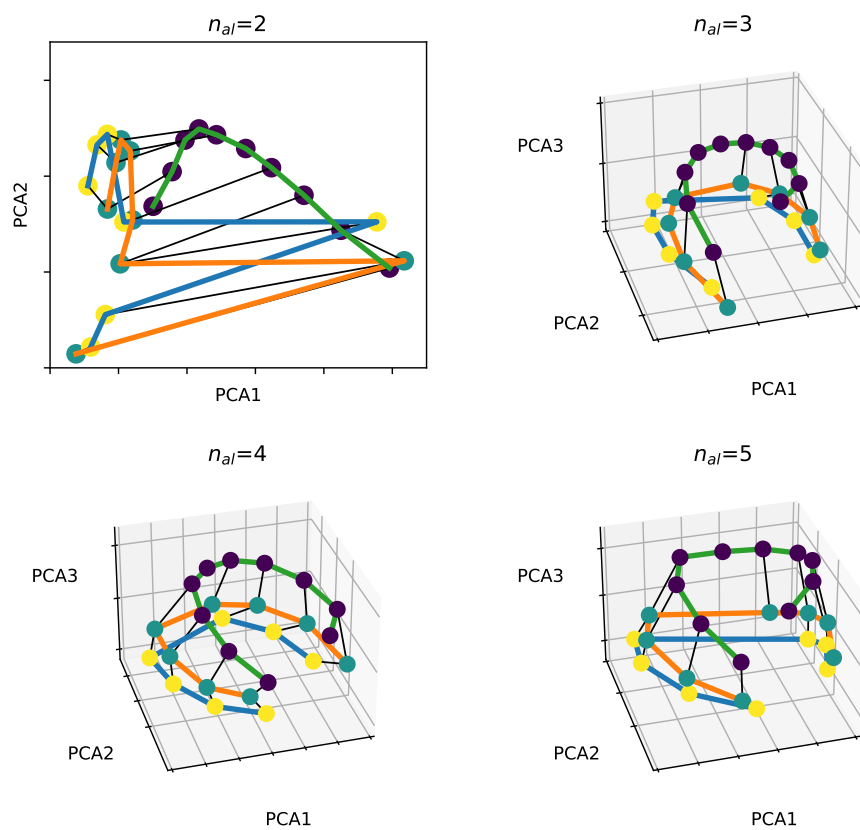


Figure S4. Comparison of converged alchemical weights matrices \mathbf{u}_{alch} for different number of alchemical channels ($n_{\text{alch}} = 2, 3, 4, 5$) represented in principal components space for the $V^{(\text{aeb})} + V^{(3\text{B})}$ models. The periods are highlighted with orange, blue and green lines, and the columns are indicated by black thin lines.

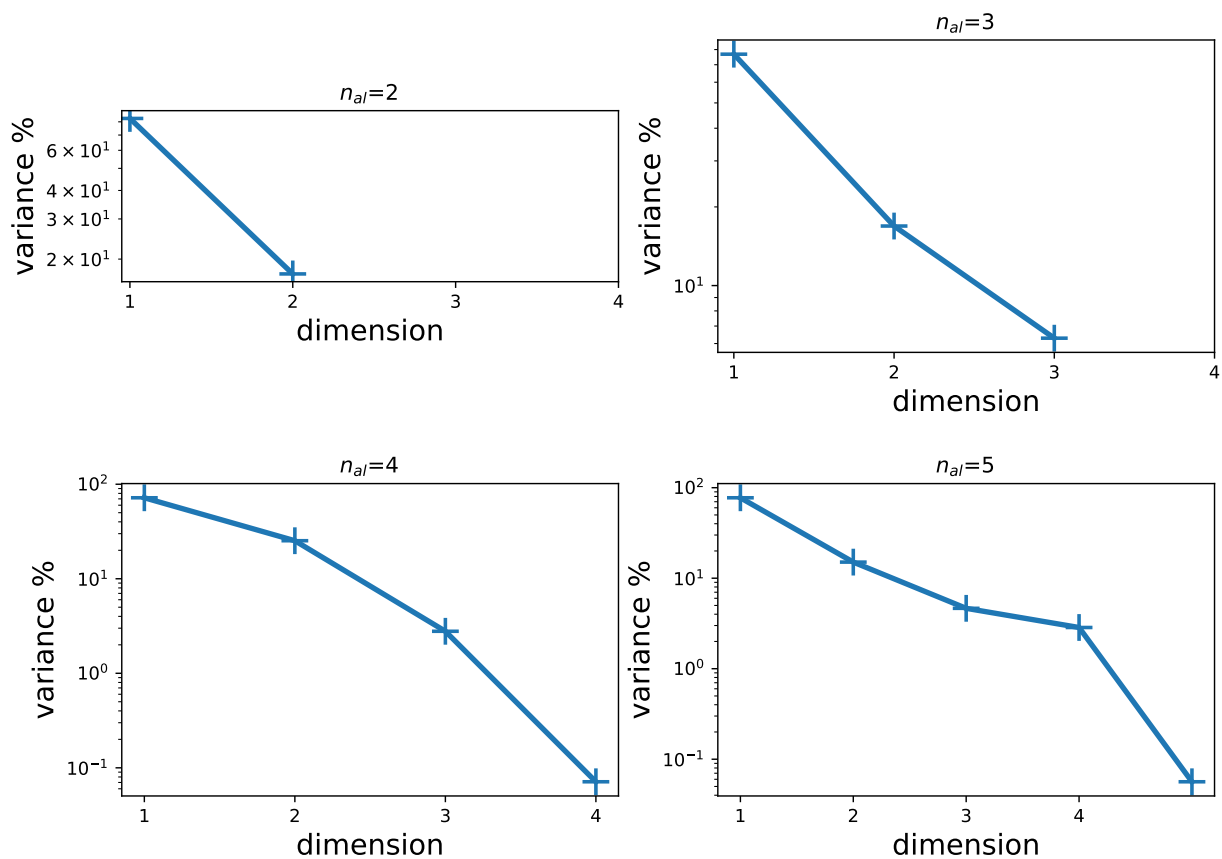


Figure S5. Comparison of the decay of the explained variance for a different number of alchemical channels ($n_{alch} = 2, 3, 4, 5$) represented in principal components space for the $V^{(aeb)} + V^{(3B)}$ models.

B. Alchemical interpolation

Exploiting the interpretability of the alchemical weights, we interpolated linearly the weights for not represented elements Re and Os, as discussed in the main text. We determined the weights for $V^{(\text{aeb})}$ (that are not contracted) by fitting the residual errors with a two-parameter model. Here we provide a parity plot between reference and predicted energies for a clearer picture (Fig. S6).

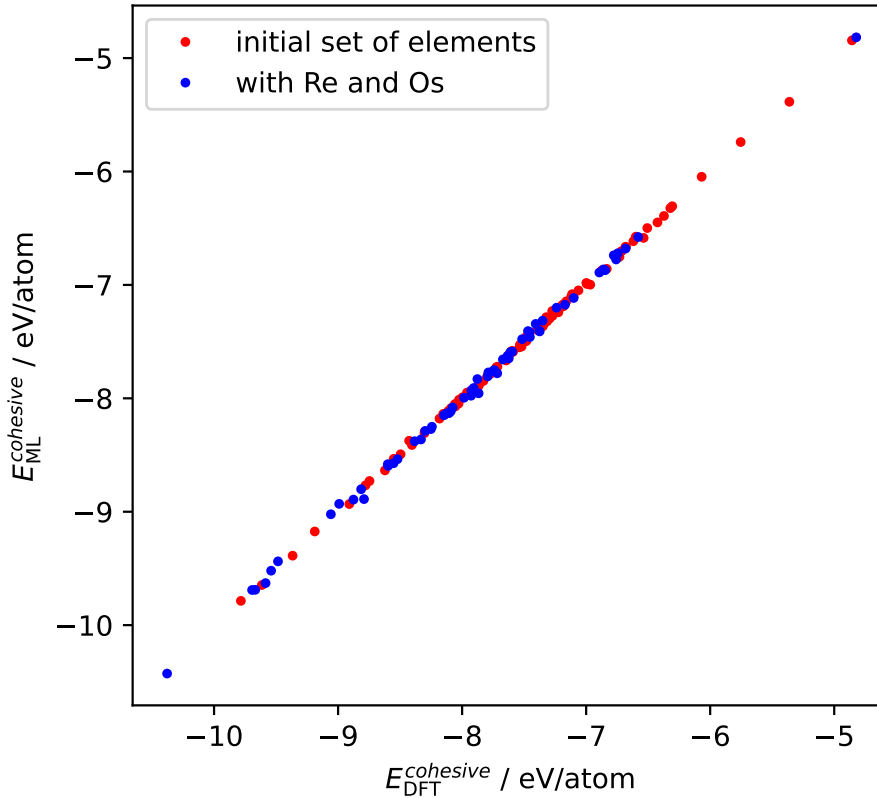


Figure S6. Parity plot between energies computed with DFT and predicted with the $n_{\text{alch}} = 4 V^{(\text{aeb})} + V^{(3\text{B})}$ model. In red are depicted the points corresponding to 60 structures from the hold-out fraction of HEA25 dataset. We randomly substituted some atoms with Re and Os, re-computed the corresponding energies with DFT and predicted energies interpolating the weights linearly from the $V^{(\text{aeb})} + V^{(3\text{B})}$ alchemical coupling matrix. The resulting energies are plotted as blue points.

III. VALIDATION

A. Binary Convex Hull

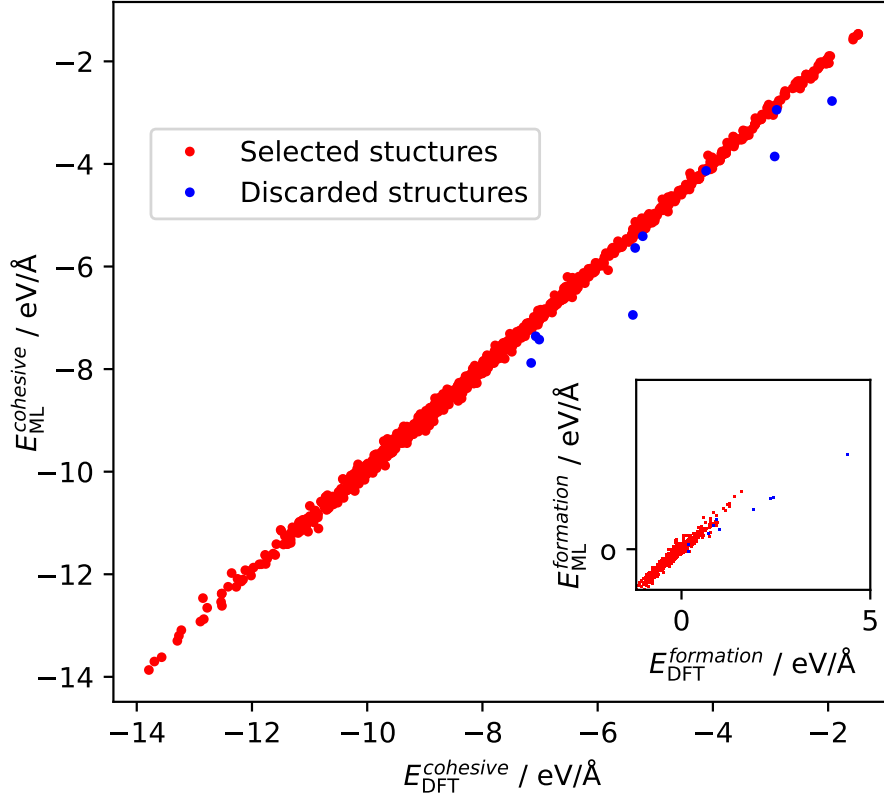


Figure S7. Parity plots between cohesive energies and formation energies (in the inset) computed with DFT and predicted with HEA25-4-NN (ML). Used in the analysis data points are depicted in red, and discarded structures – in blue.

As the HEA dataset contains only structures based on BCC and FCC crystalline lattices, for a descriptive evaluation of HEA25-4-NN performance, we discarded 10 structures out of 1415 which were too dissimilar from BCC or FCC. To measure the similarity, we computed the minimum Euclidean distance in the top-10 principle component space of power spectrum features to FCC or BCC ideal crystals (P^{FCC}, P^{BCC}) for each binary structure (P^i) as defined in (2). Fig. S8 illustrates the correlation between the introduced distance and the absolute difference in cohesive energies between DFT and HEA25-4-NN predictions. We set a threshold of 40, past which the structures were not considered (in blue). All the structures labeled in red were used to compute the MAE for the figures here and in the main text. The parity plot in Fig. S7 preserves the same colour scheme and demonstrates that all the outliers belong to the group of structures that bear no resemblance to those included in the HEA training dataset.

$$\text{dist.} = \min\{d[PCA_{10}(P^i), PCA_{10}(P^{FCC})], d[PCA_{10}(P^i), PCA_{10}(P^{BCC})]\}. \quad (2)$$

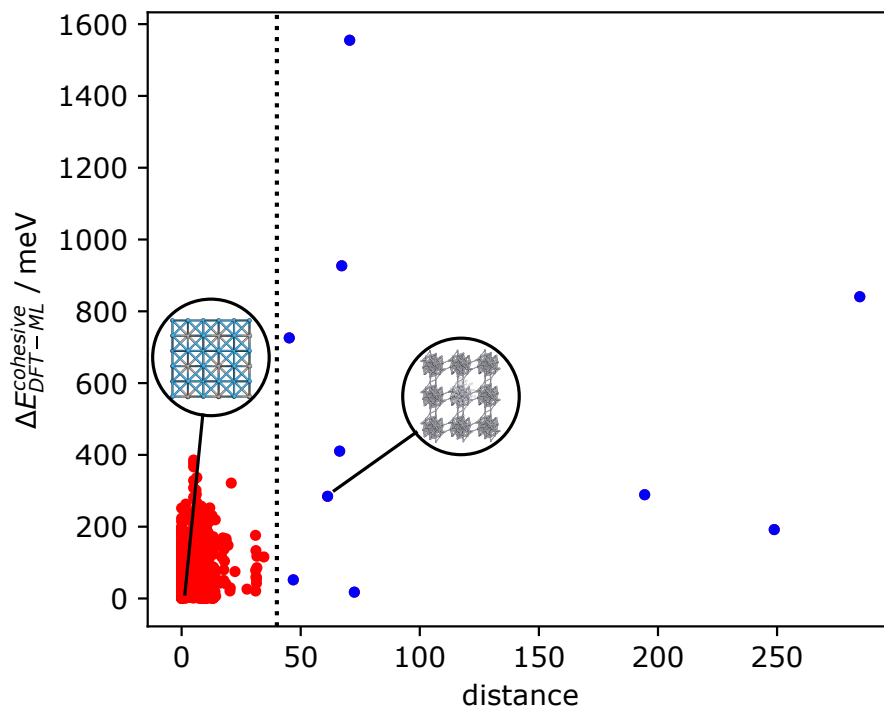


Figure S8. Correlation plot between the absolute difference in cohesive energies between DFT and HEA25-4-NN predictions and distance computed in principle component space of power spectrum features reflecting the similarity of each structure to FCC or BCC phases. The dashed vertical line, set at 40, indicates the threshold above which we discarded structures as outliers (in blue).

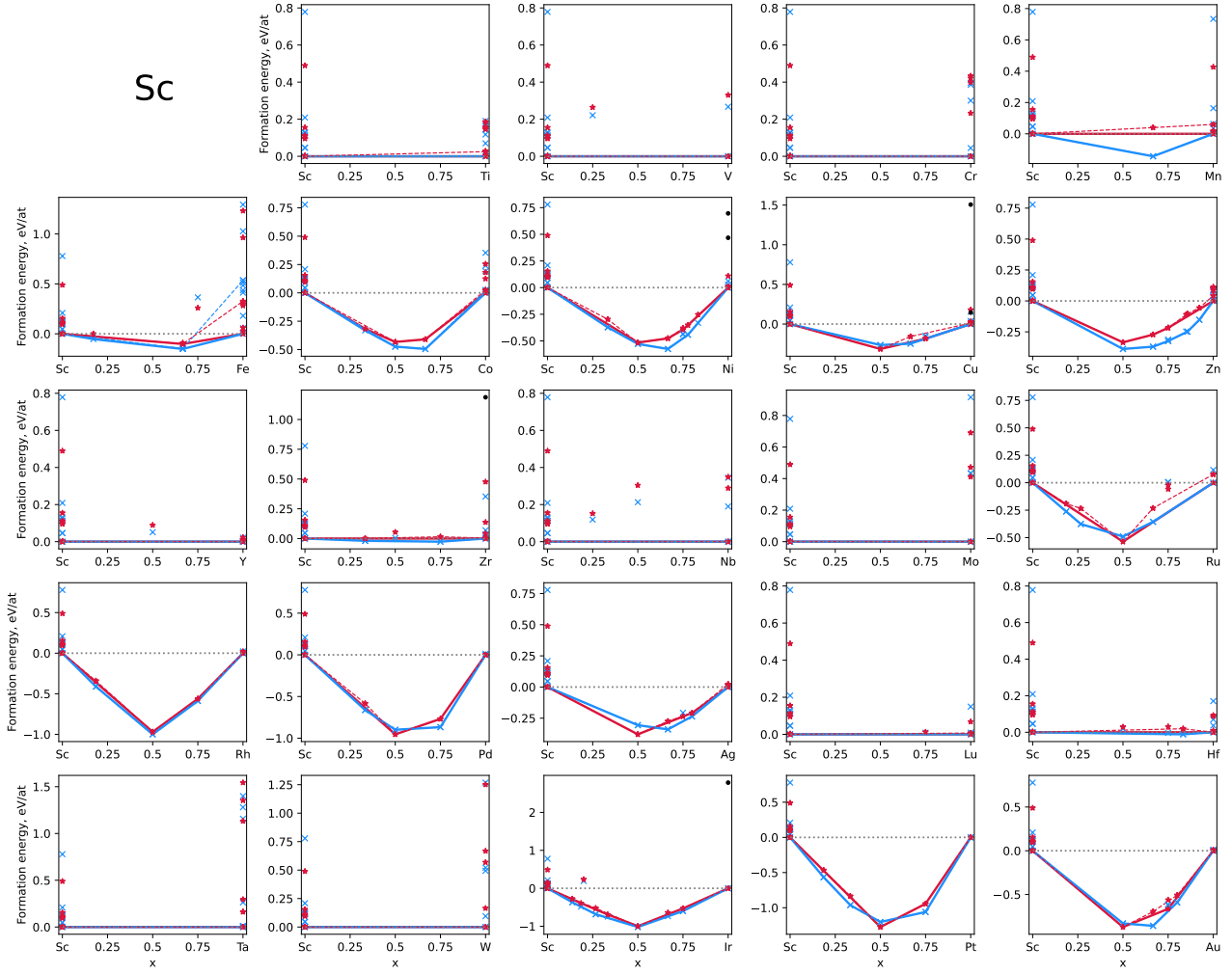


Figure S9. Hull plots for all possible pairs available within the HEA dataset with Sc. Solid lines highlight the hulls obtained from the single-point DFT calculations (blue) and the ML predictions (purple). The dashed line identifies the structures that are stable based on the energies available in the Materials Project database. Black points reflect discarded structures based on the distance measure reflecting the similarity to BCC or FCC phases. The full list of convex hulls is included the very end of this document in Sec. VI

B. Reference results with M3GNet

We report here result obtained with M3GNet⁶, a universal force-field trained on DFT data. We found the energies predicted by M3GNet to be offset from our DFT calculations by a constant factor of -438 meV/atom, which we correct for in the figures below. The error on the validation set is 15 times larger than that of HEA25-4-NN for the energy, and 2 times larger for the forces, and in almost every test we consider the error of M3GNet is much higher than that of HEA25-4-NN. It is important to consider that M3GNet targets an even broader portion of the periodic table, and that its training set of M3GNet is computed with different DFT details than ours, and so part of the error might be due to this discrepancy.

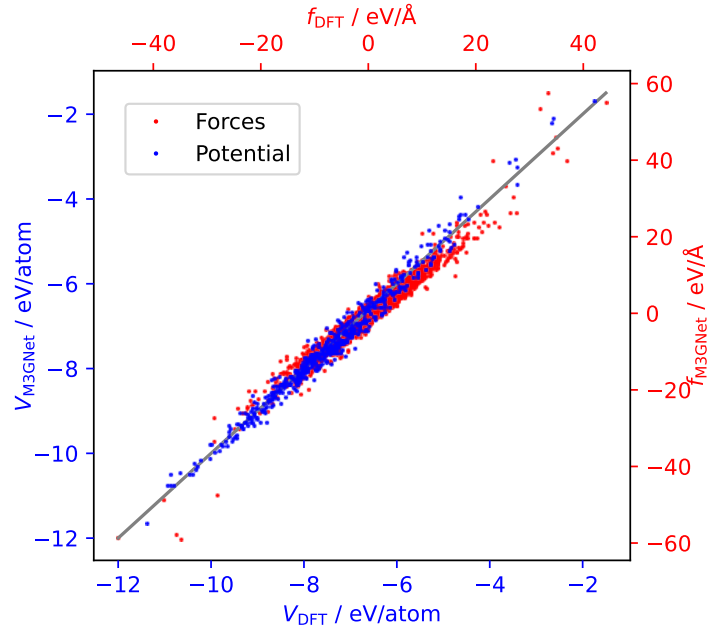


Figure S10. Comparison between the potential energy evaluated by M3GNet and DFT for the 500 hold-out structures used in the main text. A constant offset of -438 meV/atom has been applied to remove the constant shift in predicted energies compared to DFT. The energy MAE is 158 meV/atom, and the force MAE is 387 meV/Å.

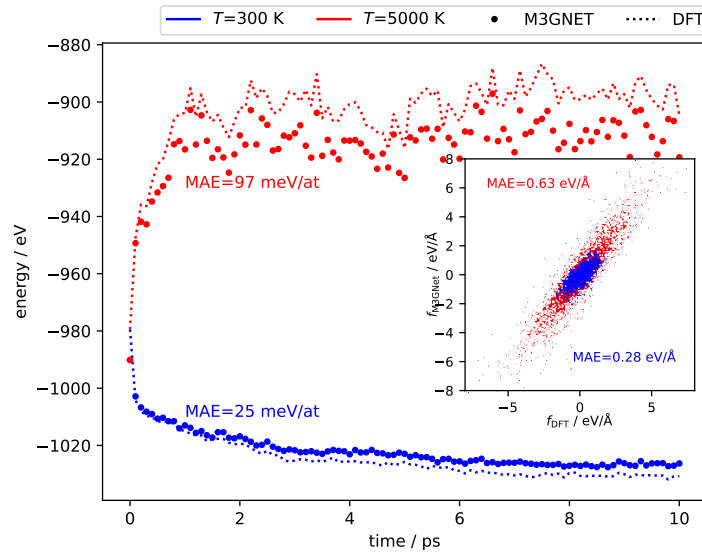


Figure S11. Comparison between the potential energy evaluated by M3GNet and DFT for the 100 snapshots of the same trajectories used in the main text. A constant offset of -438 meV/atom has been applied to remove the constant shift in predicted energies compared to DFT. The inset shows a parity plot for the force components computed for those structures. Energies have a MAE of 25 (97) meV/atom and forces a component MAE of 0.28 (0.63) eV/Å for the 300 (5000) K trajectory.

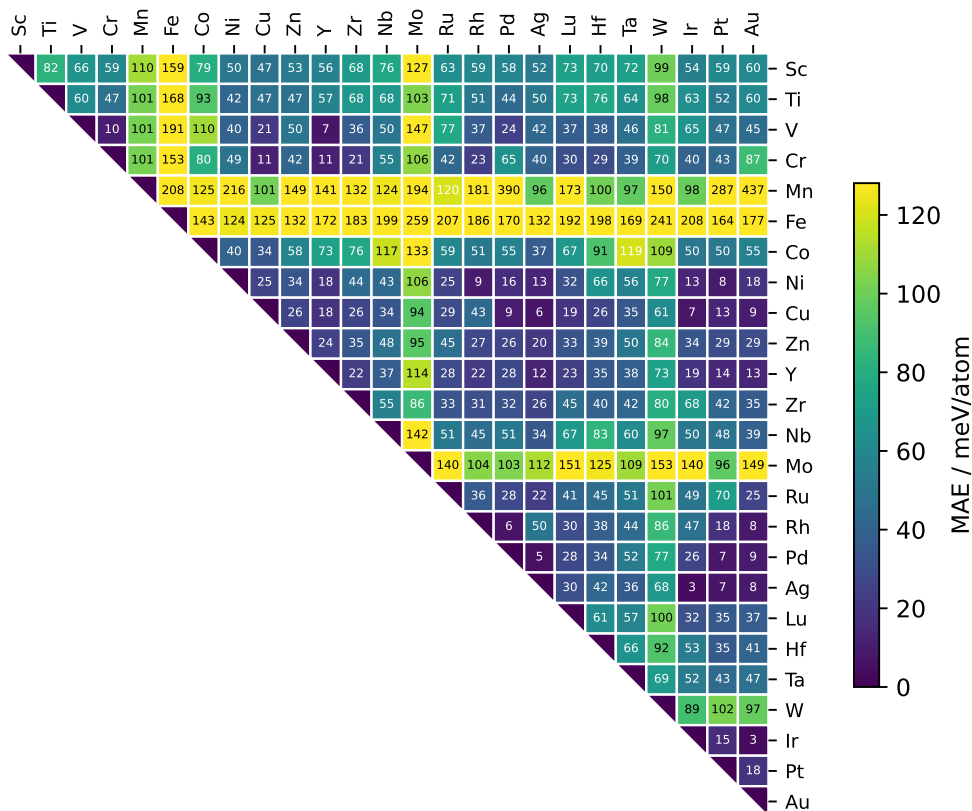


Figure S12. MAE for the formation energy of binary compounds from the Materials Project database as predicted by M3GNet, similar to the corresponding figure in the main text.

IV. CONVERGENCE OF SIMULATIONS FOR THE HEA_{all} SYSTEM

As discussed in the main text, it is a challenge to converge the simulations for the HEA_{all} system, and even the REMD/MC accelerated-sampling setup we use is not able to reach a plateau for the potential energy of the system. It is also important to consider the impact of finite-size effects on the results of the simulations: a too small simulation cell may prevent precipitation as there are not enough atoms to form a critical nucleus.

A. Equilibration

In order to verify that finite simulation length does not affect the qualitative observations we make on the affinity between the different elements, we perform simulations with a smaller box containing 125 atoms, that is both faster to run and easier to equilibrate, thanks to finite-size effects that prevent the formation of clear-cut separate phases. Fig. S13 shows that even for this smaller box, and for 500'000 REMD/MC steps (amounting to 16 million energy evaluations) energy is not fully converged.

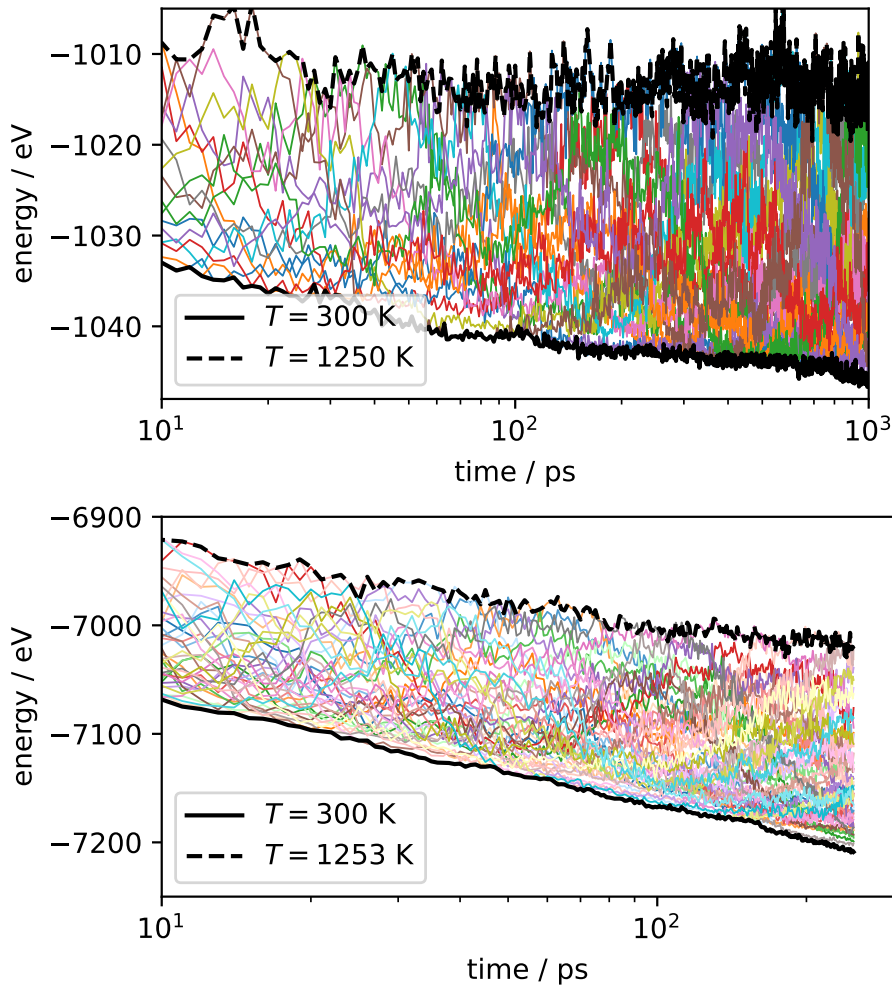


Figure S13. Trajectories of the potential energy for the HEA_{all} system with a 125-atoms box (top) compared with a 864-atoms box (bottom). The different trajectories correspond to 16 (40) replicas evolving with a combination of MD/MC steps, and parallel-tempering energy exchanges. The time scale refers to the MD integration time.

However, pair correlation functions are well-defined and weakly dependent on the starting conditions (Fig. S14). As a consequence, also the RPPs computed for the six independent trajectories are qualitatively in agreement, although they differ by as much as 0.5 units for the low-temperature replicas. High-temperature results are instead very consistent, with discrepancies below 0.05 units.

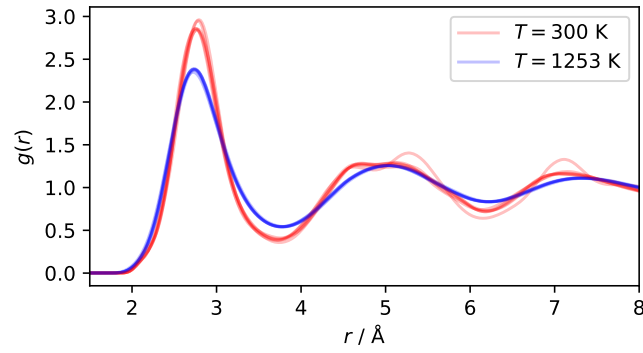


Figure S14. Plots of the total pair correlation function for the low (300 K) and high (1253 K) replicas of a REMD/MC simulation of a 125-atoms box of HEA_{all}. The lines correspond to six independent runs, each 1 ns long, with the first 100 ps discarded for (pre)-equilibration.

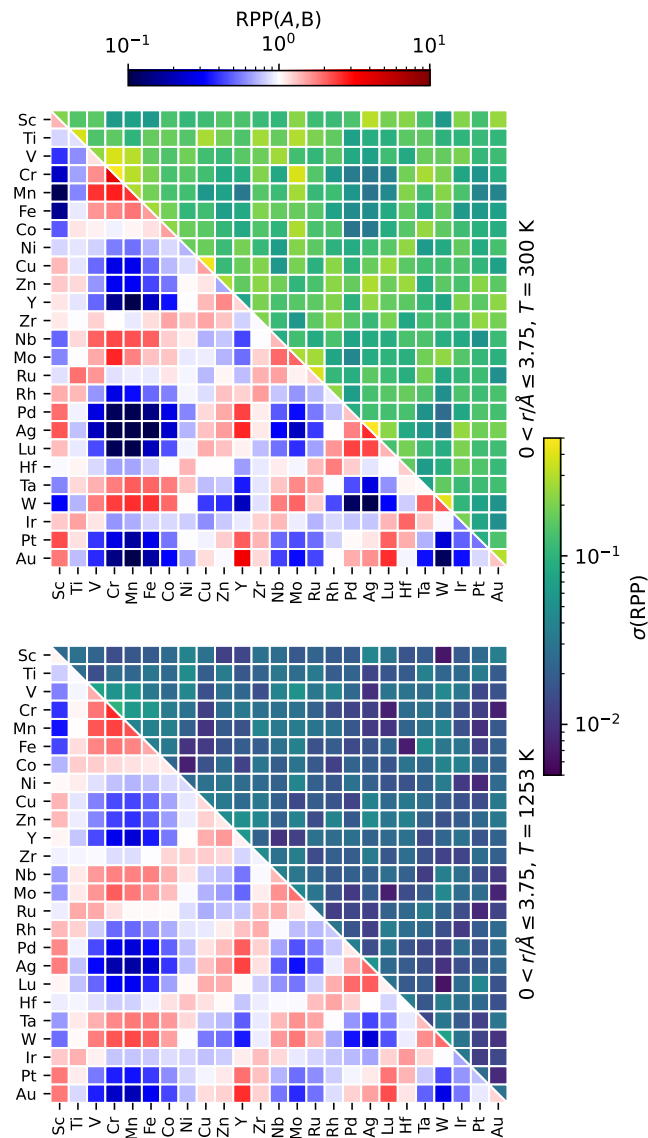


Figure S15. Short-range relative pair probabilities for a 125-atoms box of HEA_{all}, obtained by averaging 6 independent trajectories. The upper-right corner of each panel shows the standard deviation of the RPPs between the 6 trajectories.

B. Finite-size effects

Comparing Fig. IV B with the corresponding figure in the main text, one sees that using a smaller box does not affect the short-range order, with the RPP in the first neighbor shell being equal within the statistical uncertainty to that computed for the larger supercell. On the other hand, one sees clearly the presence of finite-size effects in the third neighbor shell: whereas the 864-atoms cell shows that the long-range affinity of species is weaker than, but correlated to, the short-range RPPs, in the 125-atoms box one observes almost perfect anti-correlation. This is an artifact due to the small number of atoms present in the box, that leads to depletion of the species that cluster together strongly.

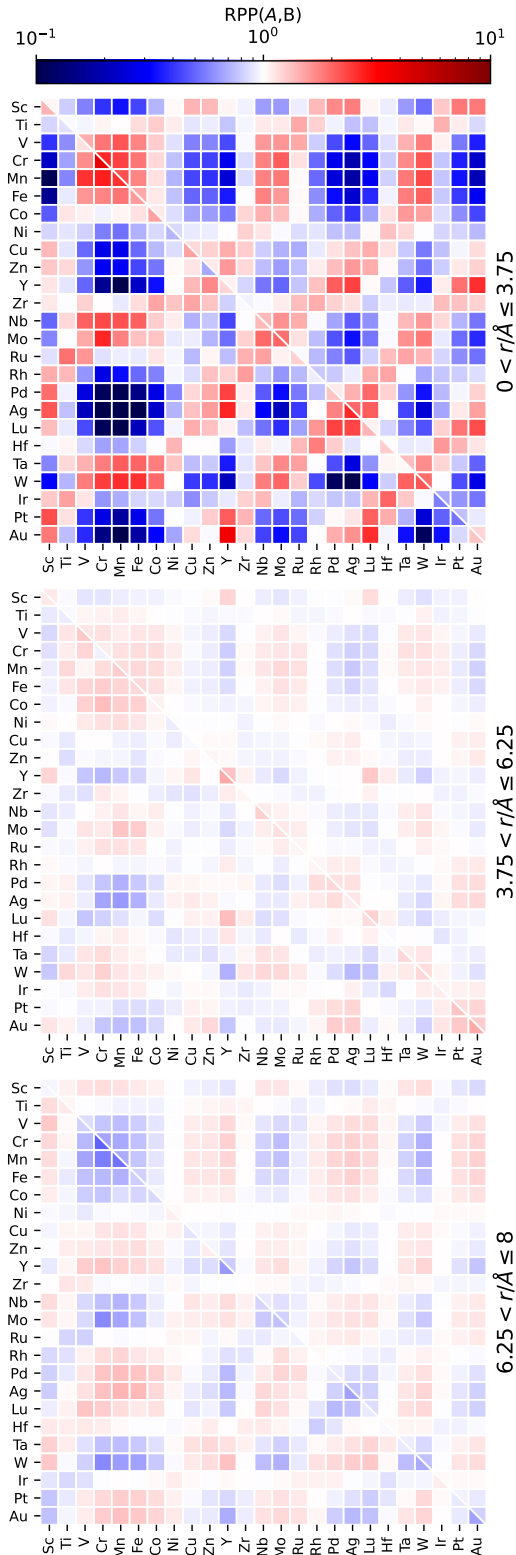


Figure S16. A plot of the relative pair probability for all atom pairs and the three regions corresponding to the first, second, and third peaks in the total pair correlation function. Each plot shows results for a 125-atoms simulations of HEA_{all} at both 300 K (lower-left corner) and 1253 K (top-right corner), averaged over the trajectories and discarding the first 100 ps (50'000 combined MD/MC steps).

V. FURTHER INFORMATION ON SIMULATIONS OF HIGH-ENTROPY ALLOYS FOR CATALYSIS

For each of the three compositions we consider we show the pair correlation functions at $T = 300$ K and $T = 1253$ K, and the RPPs at the two temperatures and for three ranges of distances.

A. CoCrFeMnNi

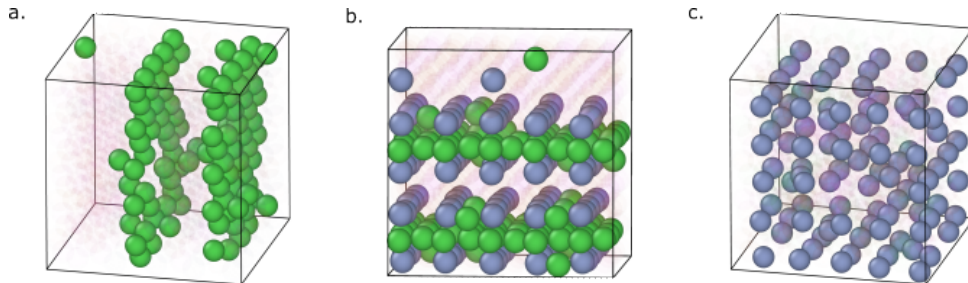


Figure S17. a. Snapshot of CoCrFeMnNi at 300 K, showing all species except Ni transparent, revealing the two Ni(100) planes, b. same snapshot rotated, showing the Ni(100) planes sandwiched by Cr-atoms (blue), and c. snapshot at 720 K with Cr atoms highlighted, revealing Cr order.

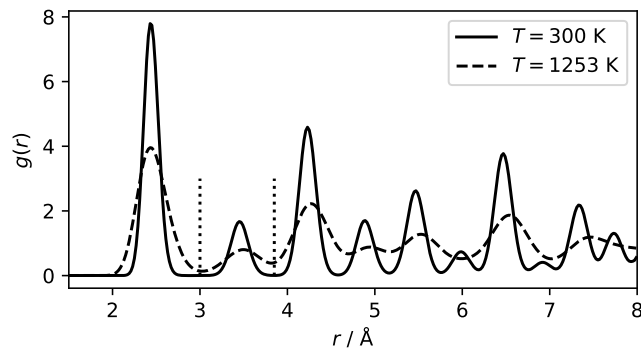


Figure S18. Pair correlation functions computed on the $T = 300$ K (full) and $T = 1253$ K (dashed lines) replicas, averaged over two independent runs of the CoCrFeMnNi system. The vertical dotted lines indicate the regions used in the definition of the pair ordering.

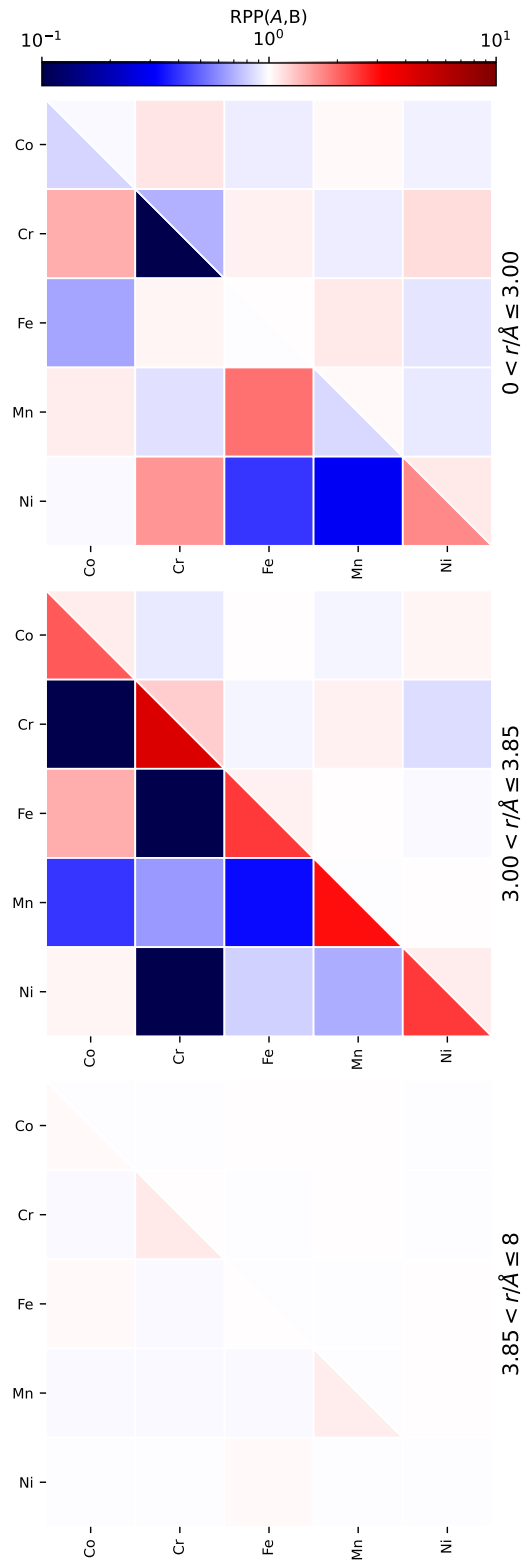


Figure S19. A plot of the relative pair probability for all atom pairs and the three regions corresponding to the first, second, and third peaks in the total pair correlation function (Fig. S18). Each plot shows results for simulations of CoCrFeMnNi at both 300 K (lower-left corner) and 1253 K (top-right corner), averaged over the trajectories and discarding the first 100 ps.

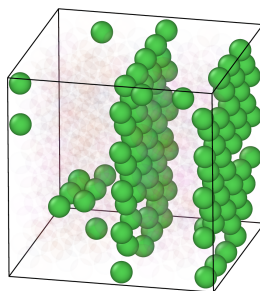
B. CoCrFeMoNi

Figure S20. Snapshot of CoCrFeMoNi at 300 K, showing all species except Ni transparent, revealing the two Ni (100) planes.

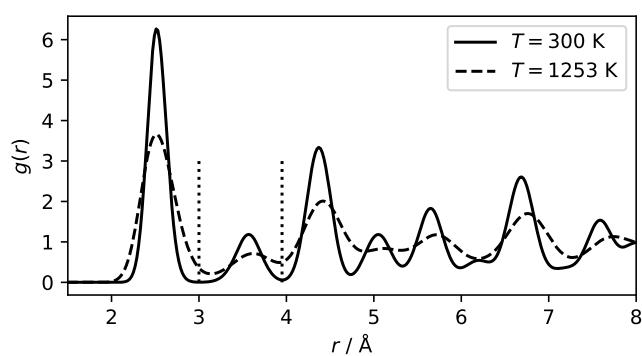


Figure S21. Pair correlation functions computed on the $T = 300$ K (full) and $T = 1253$ K (dashed lines) replicas, averaged over the eight independent runs of the CoCrFeMoNi system. The vertical dotted lines indicate the regions used in the definition of the pair ordering.

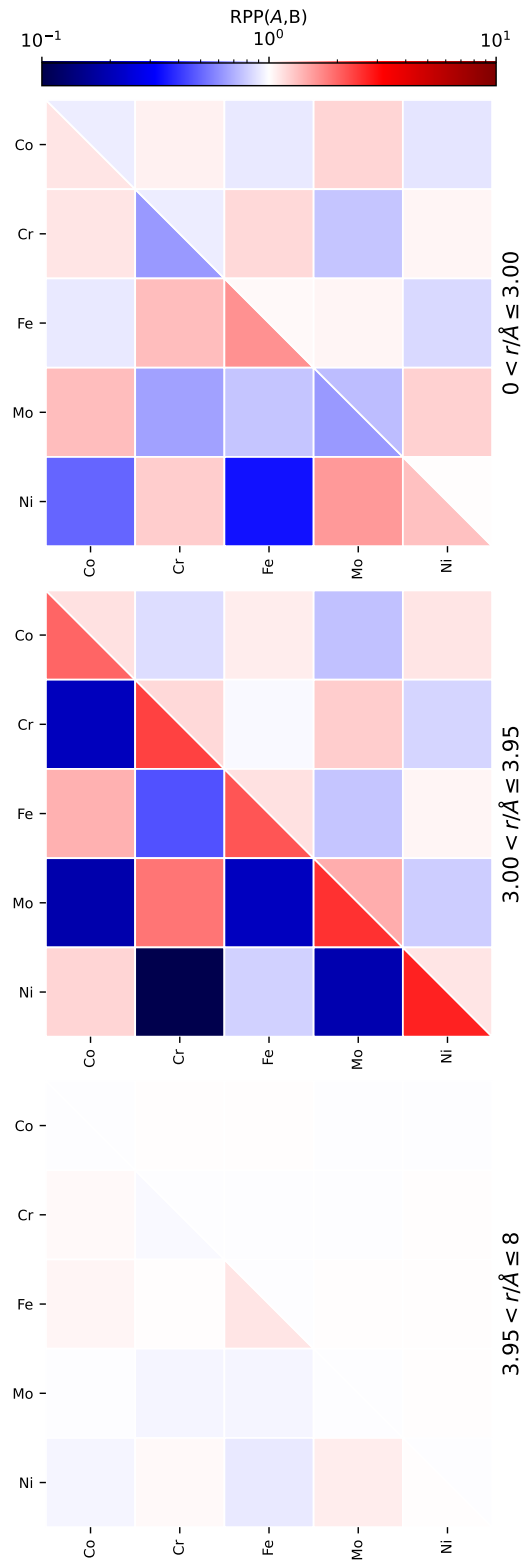


Figure S22. A plot of the relative pair probability for all atom pairs and the three regions corresponding to the first, second, and third peaks in the total pair correlation function (Fig. S21). Each plot shows results for simulations of CoCrFeMoNi at both 300 K (lower-left corner) and 1253 K (top-right corner), averaged over the trajectories and discarding the first 100 ps.

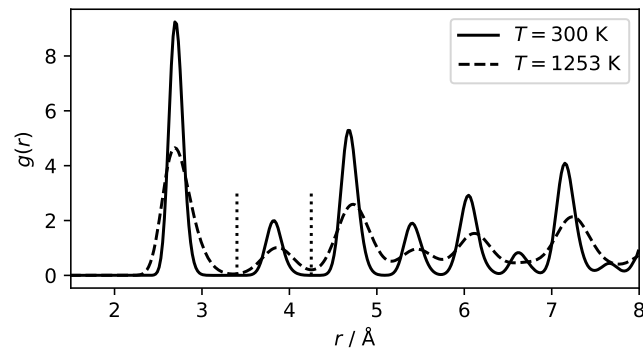
C. IrPdPtRhRu

Figure S23. Pair correlation functions computed on the $T = 300$ K (full) and $T = 1253$ K (dashed lines) replicas, averaged over the eight independent runs of the IrPdPtRhRu system. The vertical dotted lines indicate the regions used in the definition of the pair ordering.

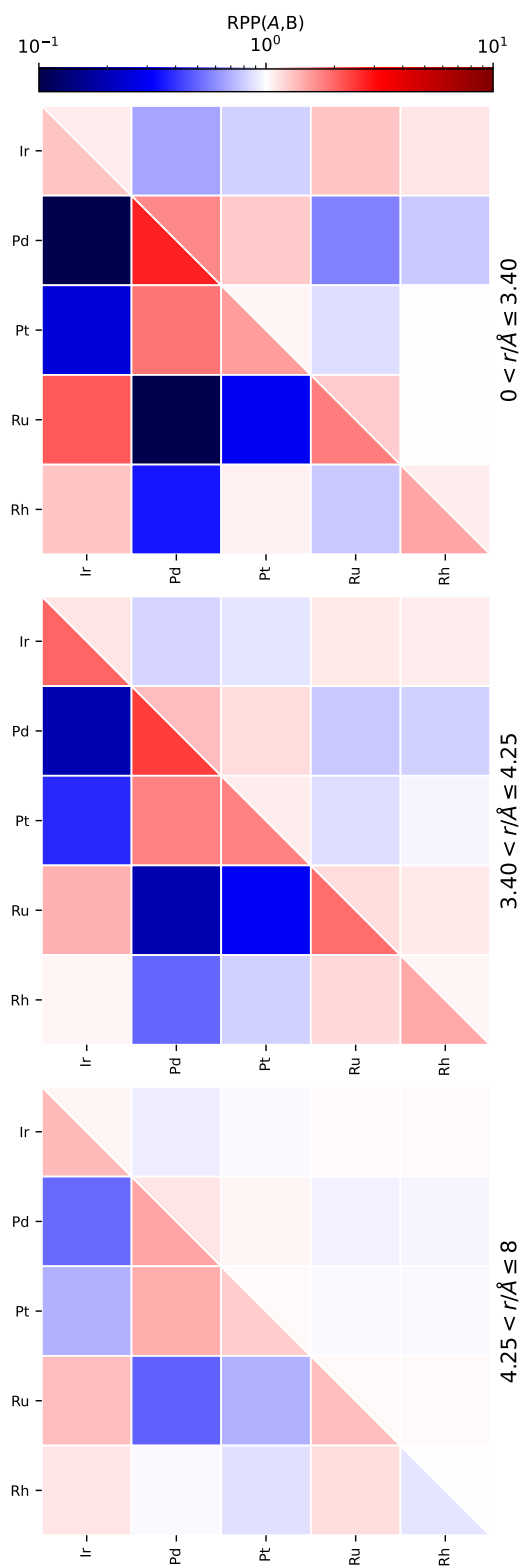


Figure S24. A plot of the relative pair probability for all atom pairs and the three regions corresponding to the first, second, and third peaks in the total pair correlation function (Fig. S21). Each plot shows results for simulations of IrPdPtRhRu at both 300 K (lower-left corner) and 1253 K (top-right corner), averaged over the trajectories and discarding the first 100 ps.

D. DFT validation of segregation in IrPdPtRuRh

In order to verify that the segregation we observe for IrPdPtRuRh is not an artifact due to the ML model, we ran similar simulations with a smaller supercell containing 180 atoms at 300 K. We performed a simulation with a simple MD trajectory, starting with a random distribution of atoms (random), and one including MC steps (swaps). After equilibration (which led to segregation in the simulation including atom swaps) we extracted 70 snapshots from both the "random" and "swaps" simulations, and re-computed their energies with the same DFT settings we used to generate the train set. It is clear that the energies are in very good agreement. There is a small near-constant shift in energies, but the relative energy of the two sets of configurations, as well as the spread within each subset, are reproduced with an accuracy comparable to that seen in the validation set. The large enthalpy gain associated with ordering is observed also in DFT calculations, which rules out the possibility that the observation of de-mixing is a consequence of errors in the ML model. We estimated the change in de-mixing free-energy due to the ML approximation using a free-energy perturbation expression, finding an error below 3meV/atom.

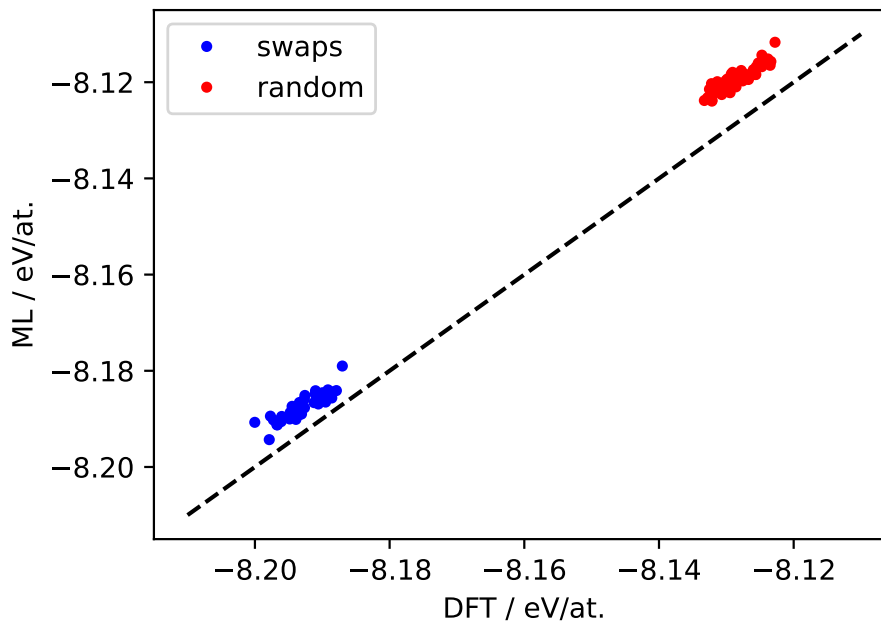
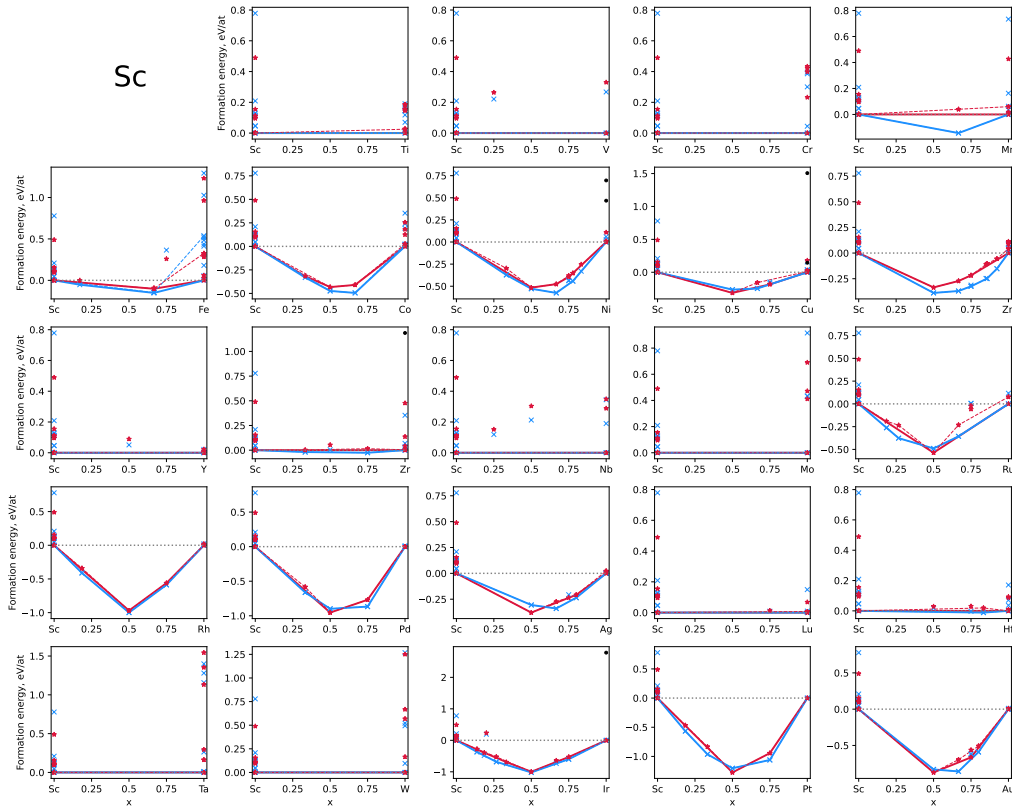


Figure S25. Parity plot of the HEA25-4-NN vs DFT energies for snapshots of a 180-atoms supercell containing IrPdPtRuRh, simulated at 300 K with plain MD (random) and including MC steps (swaps). A plot of the relative pair probability for all atom pairs and the three regions corresponding to the first, second, and third peaks in the total pair correlation function (Fig. S23). Each plot shows results for simulations of IrPdPtRhRu at both 500 K (lower-left corner) and 933 K (top-right corner), averaged over the trajectories and discarding the first 100 ps.

VI. FULL LIST OF HULL PLOTS

Below you can find a full list of convex hull plots, that extend to the full list of 25 elements the plots shown in Fig. S9. Solid lines highlight the hulls obtained from the single-point DFT calculations (blue) and the ML predictions (purple). The dashed line identifies the structures that are stable based on the energies available in the Materials Project database. Note that in many cases there is a qualitative discrepancy not only between the HEA4NN model and the Materials Project reference, but also between the Materials Project reference and the internally-consistent DFT reference. Black points reflect discarded structures based on the distance measure reflecting the similarity to BCC or FCC phases.



REFERENCES

- ¹G. Kresse and J. Furthmüller, Phys. Rev. B **54**, 11169 (1996).
- ²G. I. Csonka, J. P. Perdew, A. Ruzsinszky, P. H. Philipsen, S. Lebègue, J. Paier, O. A. Vydrov, and J. G. Ángyán, Physical Review B **79**, 155107 (2009).
- ³G. Kresse and D. Joubert, Physical review b **59**, 1758 (1999).
- ⁴H. J. Monkhorst and J. D. Pack, Phys. Rev. B **13**, 5188 (1976).
- ⁵M. J. Willatt, F. Musil, and M. Ceriotti, Phys. Chem. Chem. Phys. **20**, 29661 (2018).
- ⁶C. Chen and S. P. Ong, “A universal graph deep learning interatomic potential for the periodic table,” (2022).

